INL/JOU-22-69412-Revision-0

A combined theoretical-experimental investigation of thermal transport in low-dose irradiated thorium dioxide

December 2022

Walter Ryan Deskins, Sanjoy Mazumder, Cody A. Dennett, Kaustubh Krishna Bawane, Zilong Hua, Joshua Ferrigno, Lingfeng He, J. Matthew Mann, Marat Khafizov, David H Hurley, Anter El Azab, Amey Rajendra Khanolkar

Changing the World's Energy Future

INL is a U.S. Department of Energy National Laboratory operated by Battelle Energy Alliance, LLC

INL/JOU-22-69412-Revision-0

A combined theoretical-experimental investigation of thermal transport in low-dose irradiated thorium dioxide

Walter Ryan Deskins, Sanjoy Mazumder, Cody A. Dennett, Kaustubh Krishna Bawane, Zilong Hua, Joshua Ferrigno, Lingfeng He, J. Matthew Mann, Marat Khafizov, David H Hurley, Anter El Azab, Amey Rajendra Khanolkar

December 2022

Idaho National Laboratory
Idaho Falls, Idaho 83415

http://www.inl.gov

Prepared for the
U.S. Department of Energy
Under DOE Idaho Operations Office
Contract DE-AC07-05ID14517

Acta Materialia

A combined theoretical-experimental investigation of thermal transport in low-dose irradiated thorium dioxide

--Manuscript Draft--

Manuscript Number:	
Article Type:	Full length article
Keywords:	thermal transport; phonons; nuclear materials; irradiation; crystal defects; thermal conductivity
Corresponding Author:	Walter Ryan Deskins UNITED STATES
First Author:	Walter Ryan Deskins
Order of Authors:	Walter Ryan Deskins
	Amey Khanolkar
	Sanjoy Mazumder
	Cody A. Dennett
	Kaustubh Bawane
	Zilong Hua
	Joshua Ferrigno
	Lingfeng He
	J. Matthew Mann
	Marat Khafizov
	David H. Hurley
	Anter El-Azab
Abstract:	During reactor operation, nuclear fuels are subject to extreme temperature and irradiation conditions which can significantly degrade the fuel's thermal transport properties. The reduction in thermal conductivity of the fuel as a result of irradiation-induced lattice defects is arguably the most important property in regard to reactor efficiency and safety. For this reason, we present a theoretical investigation of thermal conductivity reduction seen in defect-bearing thorium dioxide and compare directly to experimental measurements. Phonon-mediated thermal transport of the fuel is modeled by a solution to the Boltzmann transport equation (BTE) for phonons. A cluster dynamics (CD) model for lattice defect evolution during irradiation predicts defect densities which are used as input to the BTE for modeling phonon-defect scatterings. Phonon scatterings by lattice defects include those from point defects and vacancy clusters and interstitial clusters of various sizes. The CD model is benchmarked against microstructure characterization of irradiated thorium dioxide using electron microscopy. Thermal conductivity predicted by the BTE model is compared to measured values for irradiated thorium dioxide specimens below room temperature to isolate effects of phonon-defect scattering from intrinsic 3-phonon processes, which dominate at higher temperatures. The computed conductivity values are in partial agreement at temperatures close to room temperature while slight deviations are observed at the lowest measured temperatures, suggesting that implemented phonon-defect scattering cross-section expressions may not be adequate for low temperatures. The presented work provides a necessary investigation of the influence of irradiation induced defects on fuel performance and represents a first step toward a full characterization of phonon mediated thermal transport in irradiated materials with complex microstructure.
Suggested Reviewers:	Michael Cooper cooper_m@lanl.gov

	Jeff Snyder jeff.snyder@northwestern.edu
	Patrick Hopkins phopkins@Virginia.edu
	Bolin Liao bliao@engineering.ucsb.edu

W. Ryan Deskins
School of Materials Engineering
Purdue University
West Lafayette, IN 47907
June 2, 2022

To the Editors of Acta Materialia,

Please find enclosed our manuscript titled “A combined theoretical-experimental investigation of thermal transport in low-dose irradiated thorium dioxide”. This study is a follow-up to our previous work titled “An integrated experimental and computational investigation of defect and microstructural effects on thermal transport in thorium dioxide”. Both of these investigations aim to characterize the effects of phonon defect scattering on thermal transport in thorium dioxide (ThO_2). With ThO_2 being an actinide oxide with applications in advanced energy systems, such as a potential nuclear fuel in Generation IV reactors, its thermal transport properties upon irradiation warrant further investigation to promote reactor safety and efficiency.

In our previous study, ThO_2 single crystals were exposed to 2 MeV proton irradiation which generated regions of microstructural defects of various type and concentrations. Spatial domain thermoreflectance measurements were performed to obtain thermal conductivity values of the specimens across a range of temperature from 77 to 300 K. Measurements of thermal conductivity in this low temperature regime allowed us to discriminate between intrinsic 3-phonon scattering processes (dominate at higher temperatures) and scatterings by lattice defects that are the largest contributor to thermal conductivity reduction at lower temperatures. However, it was found that at the lowest considered proton irradiation dose the thermal conductivity had already reached saturated levels where no further reduction in thermal conductivity was discernable at higher dose rates. In the present communication, we again investigate thermal transport properties in proton irradiated ThO_2 samples but at lower irradiation dose to further illuminate the dependence of microstructural evolution and thermal conductivity reduction with supplied irradiation dose. Along with investigating a wider range of irradiation conditions, our modeling of microstructural evolution has been improved by implementing a cluster dynamics method which predicts the size and concentration of crystal defect clusters ranging in sizes from point defects up to larger dislocation loops and voids. The previously used kinetic rate theory model did not allow prediction of a full spectrum of small interstitial and vacancy clusters, as it predicted only the average size of all dislocations at a single concentration. As in the previous work, we still implement a solution to the Boltzmann transport equation for phonons in the single mode relaxation time approximation in order to model phonon transport in the irradiated specimens. However, the model for phonon-defect scattering has been improved to account for scattering by intermediate-sized defect clusters as predicted by the cluster dynamics model.

Agreement between our modeled thermal conductivity and measured values is quite good at temperatures above 175 K, especially considering that only a single adjustable parameter is used in the thermal transport model. At lower temperatures our model seems to underestimate scattering of phonons by crystal defects leading to high thermal conductivity values when compared to measured values. This phenomenon seems indicative of a point defect scattering physics which are not captured by our model and warrants further investigation into thermal transport of irradiated nuclear fuels. Given the integration of experimental and modeling methods for both microstructural evolution and thermal transport of this irradiated ceramic material, we believe this work will be of interest to many of *Acta Materialia’s* readers while also extending the current knowledge of thermal transport of materials in extreme environments.

Sincerely,
W. Ryan Deskins
Anter El-Azab

A combined theoretical-experimental investigation of thermal transport in low-dose irradiated thorium dioxide

W. Ryan Deskins[1], Amey Khanolkar[2], Sanjoy Mazumder[1], Cody A. Dennett[2], Kaustubh Bawane[3], Zilong Hua[2], Joshua Ferrigno[4], Lingfeng He[3], J. Matthew Mann[5], Marat Khafizov[4], David H. Hurley[2], Anter El-Azab[1]

[1]School of Materials Engineering, Purdue University, West Lafayette, IN 47907, USA

[2]Materials Science and Engineering Department, Idaho National Laboratory, Idaho Falls, ID 83415, USA

[3]Advanced Characterization Department, Idaho National Laboratory, Idaho Falls, ID 83415, USA

[4]Department of Mechanical and Aerospace Engineering, The Ohio State University, Columbus, OH 43210, USA

[5]Air Force Research Laboratory, Sensors Directorate, Wright Patterson AFB, OH 4533, USA

Abstract

During reactor operation, nuclear fuels are subject to extreme temperature and irradiation conditions which can significantly degrade the fuel's thermal transport properties. The reduction in thermal conductivity of the fuel as a result of irradiation-induced lattice defects is arguably the most important property in regard to reactor efficiency and safety. For this reason, we present a theoretical investigation of thermal conductivity reduction seen in defect-bearing thorium dioxide and compare directly to experimental measurements. Phonon-mediated thermal transport of the fuel is modeled by a solution to the Boltzmann transport equation (BTE) for phonons. A cluster dynamics (CD) model for lattice defect evolution during irradiation predicts defect densities which are used as input to the BTE for modeling phonon-defect scatterings. Phonon scatterings by lattice defects include those from point defects and vacancy clusters and interstitial clusters of various sizes. The CD model is benchmarked against microstructure characterization of irradiated thorium dioxide using electron microscopy. Thermal conductivity predicted by the BTE model is compared to measured values for irradiated thorium dioxide specimens below room temperature to isolate effects of phonon-defect scattering from intrinsic 3-phonon processes, which dominate at higher temperatures. The computed conductivity values are in partial agreement at temperatures close to room temperature while slight deviations are observed at the lowest measured temperatures, suggesting that implemented phonon-defect scattering cross-section expressions may not be adequate for low temperatures. The presented work provides a necessary investigation of the influence of irradiation induced defects on fuel performance and represents a first step toward a full characterization of phonon mediated thermal transport in irradiated materials with complex microstructure.

1. Introduction

Thoria (ThO_2) is an actinide oxide that has gained attention lately as a potential material for advanced nuclear fuel cycles [1,2]. Also, ThO_2 has no 5*f* electron and its physical properties may be investigated as a baseline material for other actinide systems with electron correlation effects, such as the commonly used

uranium dioxide (UO_2) fuel. Regarding its use as a nuclear fuel, ThO_2 and its mixed oxides (i.e. $U_xTh_{1-x}O_2$) possess superior physical properties when compared to UO_2, such as higher melting point, lower coefficient of thermal expansion, and higher thermal conductivity [3]. This latter property is of utmost importance regarding nuclear fuel performance as thermal transport is the physics basis for electrical energy conversion of nuclear reactors. However, during operation the fuel is exposed to extreme environmental factors such as high levels of radiation and temperatures which induce microstructural changes leading to fuel degradation and reduced thermal conductivity [4]. This reduction of conductivity ensues as the primary heat carriers within the fuel (phonons) are scattered by irradiation induced point and extended defects, effectively limiting the phonons mean free path [5–7]. Despite the importance of understanding the phonon physics governing the reduction of fuel thermal conductivity during operation, the number of studies available that aim to understand this phenomenon in ThO_2 are scarce. Developing a framework for understanding of phonon-mediated thermal transport in irradiated ThO_2 is an important first step.

To investigate thermal transport in irradiated materials, it is essential to accurately characterize the microstructural evolution of the material upon irradiation which can drastically reduce its thermal conductivity during reactor operation. Nucleation and growth of small point defect clusters to extended defects in an irradiated matrix is widely studied using reaction rate theory-based models like cluster dynamics (CD) [8], e.g. the evolution of voids and loops in irradiated structural metals like α-Fe [9,10], zirconium [11], stainless steel [12,13], and tungsten [14]. However, there has been limited efforts in systematically investigating point defect and cluster densities in irradiated oxide fuels. Some significant studies are the modelling of fission gas bubble evolution [15], self-diffusion of uranium [16] and migration of xenon [17] in UO_2. However, each of these studies restrict the size of vacancy clusters in their model to small aggregates of U and O vacancies. Khalil et al. [18] presented a detailed CD model considering the stoichiometry of extended defects, i.e., SIA loops and voids in irradiated UO_2. A similar model with an accurate crystallographic description of loop and void compositions and parameters obtained from atomistic simulations has been recently been demonstrated by Mazumder et al. [19] to investigate the nucleation and

growth of defect clusters in irradiated ThO_2. Experimentally, Bawane and coworkers [20] performed full characterization of dislocation loops in ThO_2 samples irradiated at 600 °C up to 0.47 dpa. The study revealed the presence of mainly edge type faulted Frank loops ($\vec{b} = 1/3\langle 111\rangle$) along $\{111\}$ habit planes with interstitial nature in the microstructure. The present communication will focus on much lower dpa cases. Thus, only faulted Frank loops are expected as opposed to perfect loops [21,22].

While a handful of studies present first-principles-based solutions for thermal conductivity of perfect ThO_2 crystals [23,24], it is imperative to investigate conductivity reduction of ThO_2 when subjected to environmental conditions experienced during fuel operation. As such, recent works have sought insight into thermal conductivity reduction in defect-bearing ThO_2 employing either density functional theory (DFT) [25,26] or molecular dynamics (MD) methodologies [6,27–29]. These works are an essential first step in comparing experimentally measured conductivity of irradiated fuels with modeling predictions. However, a problem that persists is the difficulty of experimentally quantifying the concentrations of the smallest of defect types, such as point defects and small clusters, with which conductivity reduction through modeling can be compared [30]. This problem is compounded by the difficulties of synthesizing ceramic samples with minimized intrinsic defects [3] (i.e., impurities, porosity, and grain boundaries) which can be used as a baseline comparison to modeling before irradiation-induced defects are added. To address this gap between experimental measurements and modeling efforts for actinide oxide fuels, Dennett and coworkers [31] developed a combined experimental and modeling framework aimed at characterizing the reduction in thermal conductivity due to irradiation induced defects and applied the approach to ThO_2. In their study, high-quality ThO_2 samples were synthesized through a hydrothermal technique [3] to produce {001} oriented single crystals. These "pristine" samples were then exposed to 2 MeV proton irradiation to generate regions of defect-bearing microstructure, such that thermal transport measurements of the irradiated specimens could be measured and compared to the pristine values. Thermal conductivity measurements were performed at a number of temperatures below 300 K, such to discriminate between phonon scattering by defects and those through 3-phonon process, which take precedence at higher temperatures. Irradiation

exposures were conducted at both 20 ℃ (room temperature) and 600 ℃, where the room temperature exposure limits defect sizes and the high temperature exposure promotes the formation of larger dislocation loops. Transmission electron microscopy (TEM) was used to characterize dislocation loop sizes and concentrations, and a rate theory model [32] was implemented to predict point defect concentrations. The resulting defect profiles for each ThO_2 specimen were then input into a Boltzmann transport equation (BTE) framework [33] to predict thermal conductivity reduction in the irradiated samples and compare to measured values.

This work aims to be an extension of the work by Dennett and coworkers [31] by improving experimental and modeling methodologies and by expanding the range of irradiation conditions of the ThO_2 samples, such that the dependence of thermal conductivity reduction on dose exposure are further illuminated. In the previous work by Dennett et al., a rate theory model [32] provided point defect concentrations which was subsequently used as input into the BTE, thermal transport model of conductivity [33]. The simplicity of the previously applied rate theory model does not allow capturing a full spectrum of small interstitial and vacancy clusters as it only represents an average for all dislocation loops into a single size and concentration [21]. To improve upon the prediction of defect population in the irradiated ThO_2 specimens, we implement a cluster dynamics (CD) model capable of tracking different microstructural evolution owing to the imposed irradiation dose and temperature [18]. This allows for the prediction of defect concentrations and sizes ranging from point defects up to extended defects such as dislocation loops and voids. Also, the aforementioned work found that the thermal conductivity of ThO_2 samples irradiated at 600 ℃ and 0.16 displacements per atom (dpa) had reached saturated levels, and no further evolution of temperature dependent conductivity was observed at 0.47 dpa, despite having received nearly three times the irradiation dose. Thus, this work investigates lower dpa cases to further explore the dependence of conductivity reduction with irradiation dose in ThO_2. The TEM imaging has been improved here by implementing rel-rod dark field technique [20,21] which isolates Frank loops in the microstructure versus the previously used bright field imaging technique [5,31]. This has the benefit of providing more accurate Frank loop number

densities and size distributions with which the CD model may be benchmarked. Furthermore, we analyze temperature-dependent thermal conductivity for five ThO_2 samples (two irradiated at room temperature and three irradiated at 600 °C) with varying dose rate, compared to only two such curves (both at 600 °C) presented by Dennett et al [31].

The present work is organized as follows. Section 2 provides the methodology for each component of the implemented experimental and theoretical framework. Section 2.1 provides description of the experimental methods, including crystal growth, ion irradiation, temperature dependent diffusivity measurements, and TEM imaging for dislocation loop characterization. Section 2.2 presents both the general theory of the CD method and the parameterization specific to the model for ThO_2. Details of the BTE modeling for thermal transport in pristine and defect-bearing ThO_2 are presented in Section 2.3. Section 3 provides the results for the corresponding subsections of Section 2. Section 3.1 presents experimental results of thermal diffusivity and conductivity measurements as well as dislocation loop characterization. Section 3.2 shows results of the CD model for defect evolution in ThO_2 under irradiation, and Section 3.3 presents our BTE modeling results for thermal conductivity in the irradiated specimens. Discussion of our thermal conductivity results can be found in Section 4 and concluding remarks are given in Section 5.

2. Methodology

2.1. Experimental

Single crystals of thorium dioxide (ThO_2) were synthesized using aa hydrothermal growth technique [3]. Details relating to the feedstock material and process parameters associated with the crystal growth method have been reported previously [5]. The hydrothermally-grown ThO_2 crystals were thoroughly rinsed with deionized water and acetone to remove excess feedstock powder and residual mineralizer from the crystal surface. The (001) crystal planes were identified from the morphology of the crystals and the angle between crystal facets. The ThO_2 crystals were mounted on copper blocks using silver paste with the (001) plane parallel to the surface of the holder for subsequent irradiation and thermal conductivity measurements.

Ion irradiation was performed using the 3 MV Tandem Pelletron accelerator at Texas A&M University. The (001) faces of two mounted ThO_2 crystals were exposed to 2 MeV protons (H^+ ions) at room temperature, while another three crystals were exposed to the proton beam at 600°C. The ion beam was raster scanned with a 20% overscan of each crystal face to ensure a uniform dose across the sample surface with a flux of 1.8×10^{13} ions/cm^{2}s. The sample stage was titled by ~5° during ion irradiation to minimize channeling effects. A summary of the irradiation conditions and labels assigned to each of the five samples is provided in Table 1. The temperature of the sample was monitored during irradiation using a thermocouple press-fit to the copper mounting block. Monitoring the sample temperature using the thermocouple enabled temperature control for the irradiations at 600°C, as well as ensured no significant heating of the sample occurred during irradiations at room temperature. The depth distribution of atomic displacement damage introduced by the energetic proton beam in the ThO_2 lattice was calculated using the Stopping Range of Ions in Matter (SRIM) code in the full cascade mode [34,35] using the room temperature theoretical density of ThO_2 and atomic displacement energies of E_d = 48.5 eV and 17.5 eV for thorium and oxygen, respectively [36]. Target ion fluences were selected in the range of 4.4×10^{16} ions/cm^2 to 1.1×10^{17} ions/cm^2 for room temperature irradiations and 1.1×10^{17} ions/cm^2 to 1.1×10^{18} ions/cm^2 for ion irradiations at 600°C. The selected ion fluence range for the room temperature and the 600°C irradiations were an order of magnitude lower than the corresponding proton beam fluence range for irradiations at the same temperature in previous investigations of radiation effects on thermal transport in ThO_2 where a drastic reduction in thermal conductivity that was relatively independent of radiation dose was observed for irradiations at room temperature and 600°C [5,31]. The rationale for selecting these 'low dose' irradiation conditions was to systematically study the effect of microstructural defects on thermal transport during the early stages of damage accumulation and capture gradual reduction in thermal conductivity with dose at the onset of defect generation and clustering in the low dose regime. Fig. 1 illustrates the SRIM-calculated lattice displacement damage dose as a function of depth from the surface of the crystal due to irradiation with energetic protons. The damage profile reveals a relatively flat 'plateau' region up to ~18

μm in the depth, followed by peak displacement at ~24 μm in the depth. The displacement damage dose (in units of displacements per atom, dpa) was averaged over the 18 μm plateau region for each sample exposed to room temperature and 600°C irradiations and is listed in Table 1. The plateau damage dose for the two room temperature irradiated samples was 0.004 dpa and 0.01 dpa, while the corresponding dose for the three samples irradiated at 600°C varied between 0.01 dpa and 0.1 dpa.

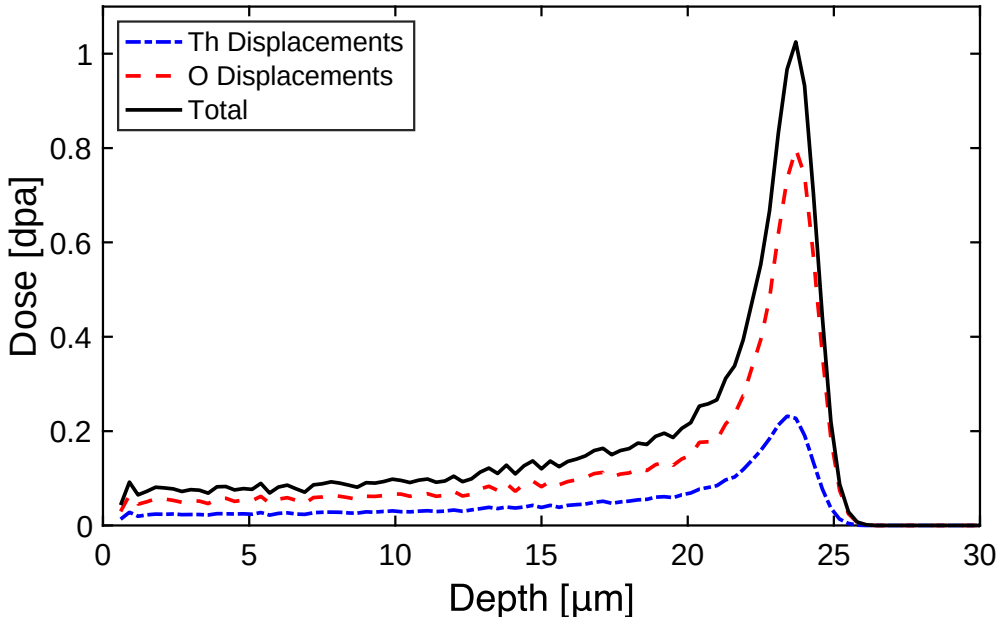

Fig 1. Lattice displacement damage dose profile computed using SRIM for 2 MeV protons in ThO_2 showing the Th and O sublattice displacements as well as total dose for the highest applied fluence, 1.094×10^{18} ions/cm^2.

Table 1. Summary of proton irradiation conditions including sample ID, irradiation temperature, ion fluence, and total dose received over the 18 μm 'plateau' region in dpa.

Sample ID	Irradiation Temperature	Ion Fluence (ions/cm^2)	Average Dose over 18 μm depth (dpa)
Pristine	-	-	-
RT01	20°C	4.375×10^{16}	0.004
RT02	20°C	1.094×10^{17}	0.01
HT01	600°C	1.094×10^{17}	0.01
HT02	600°C	3.279×10^{17}	0.03
HT03	600°C	1.094×10^{18}	0.1

Steady-state photoluminescence (PL) and spectroscopic ellipsometry measurements of the optical properties of the ion irradiated ThO_2 single crystals were performed, following the approach adopted

previously for ThO_2 single crystals irradiated to higher dose levels [37]. A 532 nm (2.33 eV) continuous wave (CW) laser was used for photoexcitation in the PL measurements. PL peaks and the optical absorption bands observed in the spectra measured on the irradiated ThO_2 crystals were attributed to creation of new electronic states emerging from charged and neutral oxygen vacancy defects created by atomic displacement damage [31,37]. Therefore, these optical spectroscopy techniques provide an indirect means to characterizing the population of oxygen anion vacancy defects at the earliest stages of damage accumulation that cannot be readily imaged using electron microscopy.

Following the optical spectroscopy measurements, temperature-dependent measurements of the thermal diffusivity in the pristine and ion irradiated ThO_2 single crystals were performed using the spatial-domain thermoreflectance (SDTR) technique [38]. In this method, an intensity-modulated continuous wave (CW) laser with a wavelength of 660 nm was sent through a confocal lens pair (of focal length 150 mm) and focused to an ~2 μm spot on the surface of the sample using a 50× objective lens. Absorption of the incident laser energy by the sample creates a 'thermal wave' whose penetration depth depends on the thermal diffusivity of the sample and the intensity modulation frequency of the heating laser. Changes in the sample reflectivity induced by thermal wave were detected by a second CW laser with an optical wavelength of 532 nm. This detection laser was guided along the optical axis of the objective lens using a dichroic mirror placed after the confocal lens pair. The reflected beam was collected by a photodiode whose output was sent to a lock-in amplifier that was phase locked to the modulation frequency of the heating laser [38]. The radius of the heating and detection laser spots at the surface of the sample was ~2 μm, while their incident power at the sample surface was ~1 mW and ~0.3 mW, respectively.

During the SDTR measurements, the heating laser was scanned in one dimension by ~10 μm on either side of the detection laser beam. Thermal wave phase profiles were acquired by measuring the phase lag of the thermal wave as a function of the separation distance between the heating and the detection laser beams. The heating laser was modulated at three frequencies - 50 kHz, 70 kHz, and 100 kHz. These modulation frequencies were selected to ensure that the thermal wave penetration depth was confined to the ~18 μm-

thick plateau damage region throughout the measurement temperature range [5]. Prior to thermal property measurements using SDTR, the {001} surfaces of the pristine and irradiated ThO_2 samples were coated with a ~60 nm-thick gold film using DC magnetron sputtering. The gold film acted as a transducer layer that absorbed the heating laser energy and also enhanced the thermoreflectance effect, thereby improving the signal-to-noise ratio. The thermal diffusivity of the pristine ThO_2 crystal and that of the plateau damage region in the irradiated ThO_2 samples was extracted by comparing the measured thermal wave phase profiles to those generated using a three-dimensional continuum thermal wave model. Details of the thermal wave model can be found elsewhere [38–40]. The model considers the influence of the 60 nm-thick gold film deposited on the sample surface. The room temperature thermal conductivity of this film was obtained from SDTR measurements on a reference glass (BK7) blank that was coated with the gold film along with the ThO_2 samples [31]. For extracting the thermal diffusivity of the ThO_2 samples at low temperature, the temperature dependence of the thermal conductivity of continuously-deposited gold film reported by Mason and coworkers [41] was parameterized and used in the continuum thermal wave model [31]. The thermal conductivity was calculated from the extracted thermal diffusivity using our previous measurement of the temperature-dependent heat capacity [31] and previously-reported first principles calculations of the temperature-dependent density of pristine ThO_2 [42].

Like in the case of our previous study on ThO_2 crystals irradiated with protons to higher doses [31], low-temperature thermal transport measurements were performed in the temperature range of 82 K to 300 K on the pristine and five irradiated ThO_2 samples in this work. Temperature-dependent measurements of thermal transport below 300 K allow us to distinguish contributions to phonon scattering from different types of lattice defects [31,43]. An increased contribution to phonon scattering from intrinsic 3-phonon processes makes this defect discrimination more challenging at temperatures above 300 K [31,33]. Low-temperature thermal transport measurements were performed by placing the mounted ThO_2 crystals in a liquid nitrogen-cooled optical cryostat (Cryo Industries model XEM). Additional details of the low temperature measurements can be found in reference [31].

Following the mesoscale thermal property measurements, lamellae for microstructure characterization using transmission electron microscopy (TEM) were prepared from the ThO_2 crystals irradiated at 600°C after completion of mesoscale thermal property measurements. Previous TEM characterization of ThO_2 crystals irradiated at room temperature with energetic protons at fluences of up to 1.727×10^{18} (resulting in an average plateau dose of up to 0.16 dpa) did not reveal any extended defects [5,31]. Since the highest fluence in the room temperature irradiation in this work was an order of magnitude lower than our previous study, extended defects were not expected to be present in the microstructure of the samples irradiated at room temperature, and consequently, the microstructure of these samples was not imaged using TEM. TEM lamellae were prepared using an *in situ* lift out technique in a field emission gun (FEG) scanning electron microscope (SEM) equipped with a focused ion beam (FIB) system (FEI Quanta 3D FEG Dual Beam). The orientation of the FIB lift outs was perpendicular to the as-irradiated crystal surfaces. To minimize FIB-induced damage, the TEM lamellae were cleaned in two steps using 5 kV (48 pA) and 2 kV (41 pA) ion beams for up to 3 minutes on each side. The final thickness of the FIB lamella was determined using electron energy loss spectroscopy (EELS) using a known electron inelastic mean free path in ThO_2 [44]. Imaging of radiation-induced defects in the microstructure was performed using a Thermo Scientific Titan Themis TEM operated at 200 kV and equipped with a probe corrector system. The rel-rod dark field technique imaging technique was employed to image Frank loops present in the microstructure, following the procedure described previously [20] for characterizing dislocation loops in ThO_2 crystals irradiated with protons to higher doses. This technique has been widely applied for characterizing microstructural features in irradiated face-centered-cubic materials [45–48]. The size and areal density distribution of the dislocation loops was determined from the dark field images using manual image analysis using ImageJ software [49]. The volumetric number density of dislocation loops was subsequently obtained using the areal number density and EELS-measured thickness of the lamella.

2.2 Cluster dynamics modeling of defect evolution under irradiation

To accurately model the scattering of phonons in irradiated ThO_2, we need a reasonable prediction of the density of monomers, i.e., Th_i, O_i, V_O and V_{Th} and clusters, i.e., SIA loops and voids, induced by irradiation. As discussed in the introduction, an atomistically informed cluster dynamics (CD) model by Mazumder et al. [19] has been employed to predict the nucleation and growth of defect clusters in the irradiated matrix. It is an improvement over the CD model presented by Khalil et al. [18] for a couple of reasons: including an accurate crystallographic description of the composition space of defect clusters, i.e., SIA loops and voids, and the use of model parameters, e.g., binding energy of point defects to clusters and the point defect diffusivities, which are determined from atomistic simulations and further optimized using observed densities of large loops in irradiated ThO_2 using TEM [31]. Other significant studies using cluster dynamics in irradiated oxides like UO_2 [15–17] limit the cluster size space to small aggregates of U and O point defects. Similar to the work by Khalil et al. [18], the clusters defined by Mazumder et al. [19] are denoted by (n, m) indicating the composition of Th and O defects, respectively. Consequently, the cluster composition space (CCS) of (n, m) self-interstitial atom (SIA) loops and voids have been defined based on the crystallography of the ThO_2 fluorite lattice. Each point in the CCS represents a cluster with specific composition (n, m) that can evolve into an adjacent cluster in the composition space, i.e., either shrink into a $(n-1, m)$ and a $(n, m-1)$ loop or grow into a $(n+1, m)$ and a $(n, m+1)$ by the absorption or emission of monomers. Point defects are assumed to be the only mobile species in the matrix which allows their interaction with clusters, leading to either cluster growth or shrinkage. The CD model is a set of coupled ordinary differential equations having a general form shown below and defining the evolution of clusters and monomers, as a sum of reaction rates for respective interactions.

$$\frac{dC_\theta(n,m)}{dt} = G_\theta(n,m) - S_\theta(n,m) + w_\theta^{\mathrm{f}}(n,m) - w_\theta^{\mathrm{d}}(n,m)\ ;\theta = \mathrm{L},\mathrm{V} \tag{1}$$

Eq. (1) shows the temporal evolution of (n, m) SIA loop and void (given by $\theta = \mathrm{L}, \mathrm{V}$) densities, $C_{\mathrm{L}}(n, m)$ and $C_{\mathrm{V}}(n, m)$ respectively. The rate of defect generation in the displacement cascade is given by the first

term in Eq. (1), i.e., $G_\theta(n,m)$ which is solely defined for Frenkel pairs O_i - V_O and Th_i - V_{Th} in the CD model. Although small clusters can also generate in the cascade, their production has been ignored due to relatively small density [50]. The second term given by $S_\theta(n,m)$ defines the loss of defects to microstructural sinks like dislocations and grain boundaries. Again, this is defined for point defects as they are assumed to be the only mobile defect species in the irradiated matrix that can migrate and get annihilated or absorbed at the sinks. The third and fourth terms define the formation, $w_\theta^{\mathrm{f}}(n,m)$, and depletion, $w_\theta^{\mathrm{d}}(n,m)$, respectively of (n,m) SIA loops and voids due to interaction of monomers with adjacent clusters in the CCS as discussed above.

The evolution of point defects and clusters are primarily governed by the rate coefficients of individual interactions, i.e., the rate of monomer recombination, rate of point defect absorption by clusters ($\theta = \mathrm{L}, \mathrm{V}$), and the rate of emission from (n,m) loops and voids. Diffusivity of the point defect species, $D_{\mathrm{O_i}}$, $D_{\mathrm{Th_i}}$, $D_{\mathrm{V_O}}$, $D_{\mathrm{V_{Th}}}$ and the energetics of the clustering phenomenon, i.e., the binding energy of point defects, Th_i, O_i, V_O and V_{Th} to loops and voids denoted by $E_{\mathrm{O_i}}^{\mathrm{b}}(n,m)$, $E_{\mathrm{Th_i}}^{\mathrm{b}}(n,m)$, $E_{\mathrm{V_O}}^{\mathrm{b}}(n,m)$ and $E_{\mathrm{V_{Th}}}^{\mathrm{b}}(n,m)$ are the critical parameters that define the rate coefficients of the CD model. As discussed systematically by Mazumder et al. [19], the binding energies have been computed using MD and mapped on the composition space of the respective clusters. The preferential evolution of near-stoichiometric (n,m) clusters in the CCS is a consequence of the point defect binding energies. Also, the point defect diffusivities obtained using temperature accelerated MD have been discussed in detail. Optimization of the parameters to fit the CD predicted size distribution of large loops, i.e, SIA loops having radius greater than 1 nm, to the observed size distribution in TEM yield the final set of parameters. The optimized values of defect diffusivities used by Mazumder et al. [19] are shown in Table 2. The purpose of this atomistically-informed CD model is to accurately predict the density of monomers and sub-nanometric small loops that are unresolved in TEM.

Table 2. Optimized point defect diffusivities used for the cluster dynamics prediction

	O_i	Th_i	V_O	V_{Th}
D^{o} $(\mathrm{cm}^2/\mathrm{s})$	0.266	25.34	4.74×10^{-3}	85.64

E^{m} (eV)	1	2.3	1.5	4.837

The coupled set of rate equations given by Eq. (1) indicating the evolution of SIA loops, voids, and monomers with irradiation dose have been solved using LSODE [51], a high order adaptive time-stepping solver of initial value problems for systems of ordinary differential equations.

2.3 BTE model for thermal conductivity

By considering phonons as quasiparticles, heat conduction in solids can be studied at a microscopic scale using the Boltzmann transport equation (BTE) which tracks the evolution of a system of particles in both space and time. The prediction of thermal conductivity for a defect free crystal of ThO_2 follows closely that presented by Deskins et al. [33], a summary of which will be described here. The intrinsic thermal conductivity of a material is governed by phonon-phonon scatterings which can be characterized by a relaxation time τ_{qs} defined as the average time between consecutive scattering events. The simplest approximation for the relaxation time of a phonon with wavenumber q and vibrational mode s is the single-mode relaxation time approximation (SMRT). Within the SMRT, it is assumed that all other phonon modes are in thermal equilibrium, and the relaxation time for 3-phonon processes takes the form [52]:

$$\tau_{qs}^{-1}\big|_{3ph} = \frac{\pi\hbar\gamma^2}{\rho N_0 \Omega v_{s,qs}^2} \sum_{q's'q"s"} \omega_{qs}\omega_{q's'}\omega_{q"s"} \times \left[\frac{\bar{n}_{q's'}\left(\bar{n}_{q"s"}+1\right)}{\bar{n}_{qs}+1}\delta\left(\omega_{qs}+\omega_{q's'}-\omega_{q"s"}\right)\delta_{q+q'-q",G}\right.$$
$$\left. + \frac{1}{2}\frac{\bar{n}_{q's'}\bar{n}_{q"s"}}{\bar{n}_{qs}}\delta\left(\omega_{qs}-\omega_{q's'}-\omega_{q"s"}\right)\delta_{q-q'-q",G}\right], \qquad (2)$$

where γ is the macroscopic Grüneisen parameter, ρ the mass density, N_0 for the total number of the primitive unit cells, Ω the primitive unit cell volume, and $v_{s,qs}$ is the sound velocity. Phonon-phonon scattering processes must adhere to both conservation of energy and crystal momentum and are enforced in Eq. (2) by the Dirac delta function, $\delta\left(\omega_{qs}\pm\omega_{q's'}-\omega_{q"s"}\right)$, and the Kronecker delta, $\delta_{q\pm q'-q",G}$, respectively. Here, G is the reciprocal lattice vector, which distinguishes normal ($G=0$) and Umklapp scattering processes. Consistent with Slack's model of thermal conductivity [53], we have restricted our

consideration of phonon scattering to Umklapp processes, on the premise that normal processes do not directly influence the thermal resistivity.

Solution of the BTE for phonons within the SMRT [52] recovers the kinetic theory expression for lattice thermal conductivity, k:

$$k = \sum_{qs} \frac{1}{3} c_{qs} \tau_{qs} \left(\boldsymbol{v}_g^{qs} \cdot \boldsymbol{v}_g^{qs} \right) = \frac{1}{3} \sum_{qs} c_{qs} \tau_{qs} \left| \boldsymbol{v}_g^{qs} \right|^2, \tag{3}$$

where $\boldsymbol{v}_g^{qs}$ is the phonon group velocity, and c_{qs} defines the phonon mode's lattice specific heat as:

$$c_{qs} = \left(\frac{\hbar \omega_{qs}}{k_B T} \right)^2 \frac{k_B \exp\left(\hbar \omega_{qs} / k_B T \right)}{\left[\exp\left(\hbar \omega_{qs} / k_B T \right) - 1 \right]^2} . \tag{4}$$

Brillouin zone summations for phonon-phonon scattering rates, lattice specific heat, and thermal conductivity are performed over the irreducible Brillouin zone [54,55] of the face-centered cubic lattice structure of ThO_2. Here, a uniform cubic mesh of 1299 representative q-points is used to sample the irreducible Brillouin zone. Meshing of the irreducible Brillouin zone exploits point group symmetries by assigning weighting factors to each q-point. Dispersion relations for ThO_2 are obtained through fitting of trigonometric functions [33] to inelastic neutron scattering data reported by Clausen et al. [56]. These dispersion relations provide both frequencies and group velocities for all 1299 sampled q-points, and the above quantities [Eqs. (2-4)] are found by direct summation.

In addition to intrinsic phonon-phonon scattering, phonon scattering by crystal defects such as vacancy and interstitial points defects as well as that by vacancy and interstitial clusters are mechanisms contributing to the lattice extrinsic thermal resistivity in irradiated materials. Using a second-order perturbation theory, Klemens [57] presented a general expression for what is often called the scattering parameter to quantifying phonon-point defect scattering strength in terms of the mass difference, ΔM, harmonic force constant difference, ΔK, and the elastic strain scattering due to atomic radius change, ΔR. This parameter Γ is given by:

$$\Gamma_i = \sum_i f_i \left(\frac{\Delta M_i^2}{M^2} + 2 \left(\frac{\Delta K_i}{K} - 2Q\gamma \frac{\Delta R_i}{R} \right)^2 \right), \quad (5)$$

where f_i is the fractional defect concentration of the ith defect type, and Q approximates the number of distorted nearest-neighbor bonds around the point defect (3.2 for vacancy defects and 4.2 for interstitials). The macroscopic Grüneisen parameter for ThO_2 has been assigned a value of 2 in the present study [58]. Having calculated the scattering strength Γ for a particular point defect, the relaxation time of a phonon described by wavenumber q and polarization s is written in the form [59]:

$$\tau_{PD,qs}^{-1} = \frac{\Gamma \Omega_0}{4\pi v_{s,qs} v_{g,qs}^2} \omega^4, \quad (6)$$

where Ω_0 is the average atomic volume. However, at significant off-stoichiometry due to point defects, the change in average atomic mass, volume, and force constants must be considered [43]. Gurunathan et al. [59] provides a detailed description of this, and a full description of our treatment of point defect scattering in ThO2 may be found in the work by Deskins et al. [33].

Depending on the irradiation environment of a fuel, vacancies and interstitials may cluster to form voids (spherical vacancy clusters) and interstitial dislocation loops (planar interstitial clusters) of varying sizes. Furthermore, small defects like point defects are typically modeled to scatter phonons in the Rayleigh regime where relaxation times vary as ω^4, while larger defects such as voids cause purely geometrical scattering characterized by their physical cross section, where the scattering strength is independent of phonon frequency [60]. This necessitates a treatment of phonon-defect scattering which accounts for the various size regimes of vacancy and interstitial cluster scattering. To account for phonon scattering by various size vacancy and interstitial clusters, phonon relaxation times are required which bridge the gap between point defect Rayleigh scattering and geometrical scattering by larger voids and dislocations loop. The details are presented below.

Klemens [61] provided a model for phonon scattering from dislocation loops by treating the structure of the loop as a stacking fault, which has shown surprisingly good agreement with the resulting reduction of thermal conductivity in ceramics [62]. The relaxation time associated with such loops with radius, R_d, and number density, n_d, is:

$$\tau_{loops}^{-1}(\omega) = \frac{0.7\pi a^2 \gamma^2 R_d^2 n_d}{v_{s,qs}} \omega^2 \quad (7)$$

for a crystal with lattice parameter a. However, as described in Section 2.2, the nucleation and growth of interstitial point defects into larger dislocation loops will depend on irradiation conditions of the fuel, and Eq. (7) will overestimate scattering from smaller interstitial clusters. For this reason, a model developed by Turk and Klemens [63], which represents platelet inclusions as a thin disk of height h, is implemented for phonon scattering by loops of intermediate sizes down to those just larger than dimer defects. This relaxation time model can effectively bridge the reduction in thermal conductivity for increasing sizes of interstitial cluster when implementing Eq. (6) for monomers/dimers and Eq. (7) for dislocation loops. For platelets which introduce a change in mass ΔM and a fractional volume change α within the host lattice, the associated phonon relaxation time is given by [63]:

$$\tau_{plat}^{-1} = \frac{4(hR_d)^2}{v_{s,qs}} n_d \left(\frac{\Delta M}{2M} + \gamma\alpha\right)^2 \omega^2 q^2 I(qR_d) \quad (8)$$

where $I(qR_d)$ captures the diffraction nature of scattering and is approximated by an integral over the cylindrically symmetric Bessel function [63]. Because our modeled loops are formed via clustering of interstitial defects, the change in mass fraction in Eq. (8) reduces to 1/2. Furthermore, a value of $\alpha = 0.3$, which characterizes the introduced elastic strain, was found to produce a reduction in thermal conductivity that converges with Eq. (7) at large loop sizes. Similarly, for vacancy clusters of intermediate sizes, Majumdar [64] suggested a form for scattering by spherical defects which recovers both Rayleigh like and geometrical scattering for cases of small and larger cluster sizes, respectively. For vacancy clusters with radius, R_c, and number density, n_c, the associated scattering relaxation time is given as:

$$\tau_{void}^{-1} = n_c v_g^{qs} \pi R_c^2 \left(\frac{(qR_c)^4}{(qR_c)^4 + 1} \right) \quad (9)$$

Having calculated the intrinsic 3-phonon relaxation time via Eq. (2) and the relaxation time due to point defects [Eq. (6)], interstitial clusters including dislocation loops [Eq. (8)], and vacancy clusters including voids [Eq. (9)], the total relaxation time for a given phonon mode is found using Matthiessen's rule as:

$$\frac{1}{\tau_{tot}} = \frac{1}{\tau_{3ph}} + \frac{1}{\tau_{PD}} + \frac{1}{\tau_{void}} + \frac{1}{\tau_{plat}} \quad (10)$$

For all calculations of defect-affected thermal conductivity, concentrations of point defects and concentration/sizes of vacancy and interstitial clusters are obtained from the CD model presented in Section 2.2 and parametrized based on experimental data discussed in the next section.

A previous investigation [5] on ThO_2 noted that the quality of available feedstock material can lead to variability of impurity concentrations within the bulk of unirradiated or "pristine" ThO_2 samples. These impurities have a non-negligible effect on thermal conductivity and must be accounted for to match the defect-free conductivity predicted by Eq. (3) to measured values. Thus, a general impurity scattering term is employed of the form $\tau_{imp}^{-1} = A\omega^4$, where A is treated as a fitting parameter. By considering only τ_{3ph} and τ_{imp} as active phonon scattering mechanisms, a value of $A = 6.0 \times 10^{-44}$ was found to match our model predictions to that of measured conductivities for pristine ThO_2 samples of this study. Fig. 2 shows results of our model for defect-free ThO_2 thermal conductivity, that of the fitting procedure for τ_{imp}, along with measured values from this study. This simplified approach to account for initial impurity concentrations in the pristine samples provides remarkable agreement over the entirety of the considered temperature range. For all further calculations of defect-affected thermal conductivity τ_{imp} is included in the total phonon relaxation times with the same constant value of A.

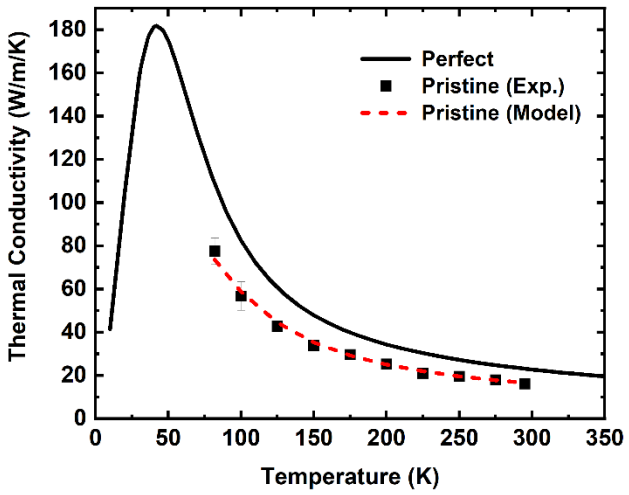

Fig. 2. Predicted temperature dependent thermal conductivity of a perfect ThO_2 crystal (solid line) and our model for the pristine ThO_2 sample (dotted line) compared to that measured (squares)

3. Results

3.1. Experimental results

Pristine ThO_2 is an optically transparent semiconductor with a wide bandgap of 5.4 eV [65]. Consequently, the photoluminescence spectra did not reveal any distinct peaks in the visible range of the electromagnetic spectrum when photoexcited with a 532 nm (2.33 eV) CW laser. The optical absorption spectra also did not show any distinct bands in the visible spectrum. The PL spectra on the irradiated ThO_2 crystals, however, revealed two distinct peaks – one at ~1.67 eV, and another sharp peak at ~1.94 eV, in agreement with PL peaks reported in ThO_2 crystals irradiated with protons to higher doses [37]. While the intensity of the 1.67 eV increased with atomic displacement damage dose, the intensity of the 1.94 eV peak monotonically decreased with irradiation dose in the samples irradiated at 600°C. The complex reflectance data measured using spectroscopic ellipsometry on the ThO_2 crystals irradiated at 600°C also showed features indicative of optical absorption at ~1.67 eV and at ~1.95 eV. This PL spectra and the corresponding complex reflectance data is presented below in Fig. 3 (a) and (b), respectively. Similar features were not discerned in the ellipsometry spectra corresponding to the room temperature irradiated ThO_2 crystals suggesting that although these optical absorption bands may be present, their intensity is too low to be detected with

sufficient accuracy. The raw reflectance data measured on ThO_2 crystals irradiated at 600°C were fitted to a 'General oscillator' model, described previously [37]. Like in the case of the PL spectra, the amplitude of the optical absorption oscillator at 1.67 eV increased with dose, while that of the oscillator at 1.95 eV increased from sample HT01 to HT02, and subsequently decreased in sample HT03.

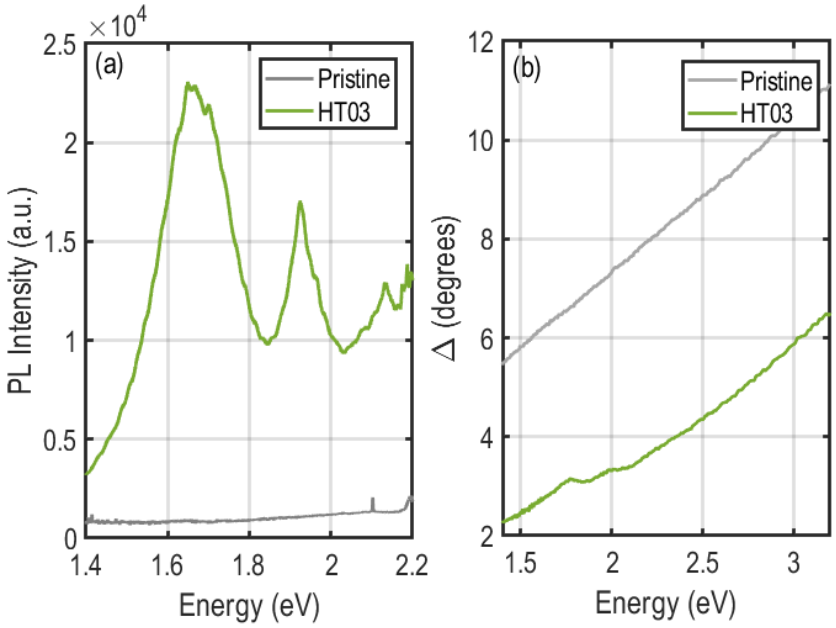

Fig. 3. (a) Measured PL spectra highlighting peaks at ~1.67 eV and at ~1.93 eV in the irradiated samples. (b) Spectral dependence of the imaginary part of the complex reflectance (Δ) measured using spectroscopic ellipsometry. Optical absorption peaks at ~1.8 eV and ~2.0 eV were observed in samples HT01 and HT02.

Fig. 4 shows weak beam dark field TEM images of the microstructure of the three ThO_2 samples irradiated at 600°C acquired by titling the samples to reach the [011] zone. Like in the case of previous observations of the microstructure of higher dose proton-irradiated ThO_2 crystals [20], bright elongated features are seen in the dark field images. These features confirm the presence of faulted Frank loops with {111} habit planes [20]. The average loop size and number density imaged in the microstructure of these three samples is summarized in Table 3. The uncertainties in loop size are given by the standard deviation in the measured radius. The corresponding uncertainties in the number density are calculated using counting statistics and assuming a 20% error [66] in the EELS-measured lamella thickness. It is evident from the summary in Table 2 that the size and density of the dislocation loops monotonically increases with applied dose. This is contrary to our previous observation of dislocation loop characteristics in the ThO_2 samples irradiated

with protons at 600°C to average doses ranging between 0.16 dpa to 0.79 dpa [31]. In the case of higher-dose irradiations, the measured loop radius was found to remain relatively constant between 2-3 nm in the 0.16-0.79 dpa dose range, while the density was found to monotonically increase between (2.6-3.5) × 10^{22} m^{-3}. It is worth noting that while the applied dose in this work is about an order of magnitude lower than that in our previous study [31], the measured loop radius distribution is only marginally lower, while the loop density is comparable to that observed in reference [31].

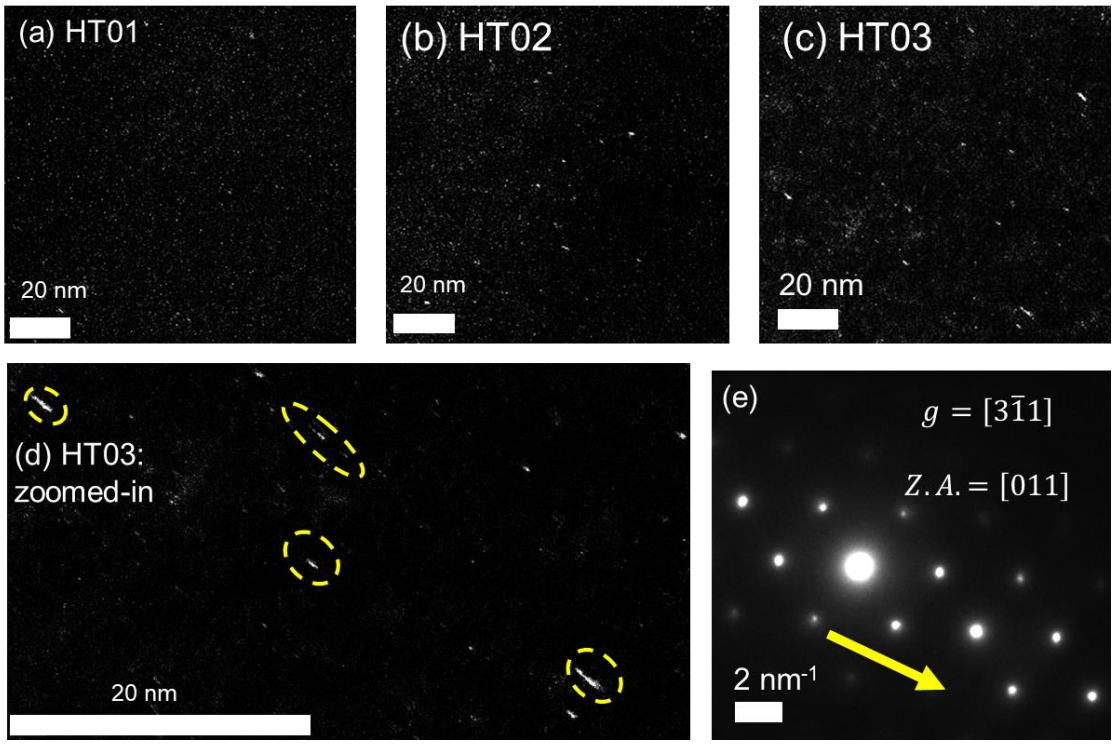

Fig. 4. Rel-rod dark field images of the microstructure of samples (a) HT01; (b) HT02; and (c) HT03. Panel (d) shows a magnified view of the microstructure of sample HT03. The highlighted bright elongated features are characteristic of faulted interstitial-type Frank loops. Panel (e) shows the diffraction pattern at Burger's vector g=[3 1-1] in two beam condition along the [011] zone axis.

Table 3. Summary of dislocation loop size and density in the microstructure of the ThO_2 samples irradiated at 600°C obtained from TEM image analysis

Sample ID	Average Dose (dpa)	Loop radius (nm)	Loop number density (× 10^{22} m^{-3})	EELS-measured lamella thickness (nm)
HT01	0.01	1.32 ± 0.41	2.35 ± 0.35	51
HT02	0.03	1.53 ± 0.59	3.13 ± 0.08	46
HT03	0.1	1.93 ± 0.98	3.21 ± 0.13	53

As stated in Section 2.1, the temperature-dependent thermal diffusivity of the pristine ThO_2 sample as well as that within the 'plateau' damage region was extracted by comparing the measured thermal wave phase profiles with those generated through a continuum thermal wave model. The average Jacobian estimate of the 2σ confidence interval on the optimized thermal diffusivity across most measurements was ~5%. For pristine ThO_2 at temperatures below 100 K this uncertainty increased to ~10% as the high conductivity results in a shallower slope of the measured thermal wave phase profile while the absolute instrument phase noise remains constant. The values of the measured thermal diffusivity represent the average of at least five measurements on different locations on the {001} face of the ThO_2 crystal at each temperature. Fig. 5(a) shows a plot of spatially averaged temperature-dependent thermal diffusivity measured on the pristine and irradiated ThO_2 samples [67]. The measured temperature-dependent thermal conductivity of all samples is shown in Fig. 5(b) [67]. The error bars in Fig. 5 represent the standard deviation of the spatially averaged measurements. Measurements on two pristine ThO_2 crystals – one with an 'as-grown' surface, and another with a polished surface – showed that the crystal surface quality had little effect on the measured thermal transport properties. As expected, the thermal diffusivity and thermal conductivity of the pristine ThO_2 crystal was found to increase with decreasing temperature and follow a ~1/T due to reduced 3-phonon scattering at low temperature. Our measurements of the temperature-dependent thermal conductivity in pristine ThO_2 are in good agreement with corresponding measured values reported previously by Mann and coworkers on similar hydrothermally-grown ThO_2 single crystals [3]. The irradiated ThO_2 crystals exhibited a significant reduction in thermal transport properties when compared to the pristine equivalent. Although the thermal diffusivity of the irradiated ThO_2 samples increased with decreasing temperature, the magnitude of this increase was only marginal. The thermal conductivity of the irradiated samples, on the other hand, remains relatively insensitive to temperature, and even marginally reduces with decreasing temperature. A similar trend in the temperature dependence of thermal conductivity was observed in ThO_2 crystals irradiated with protons to higher doses [31].

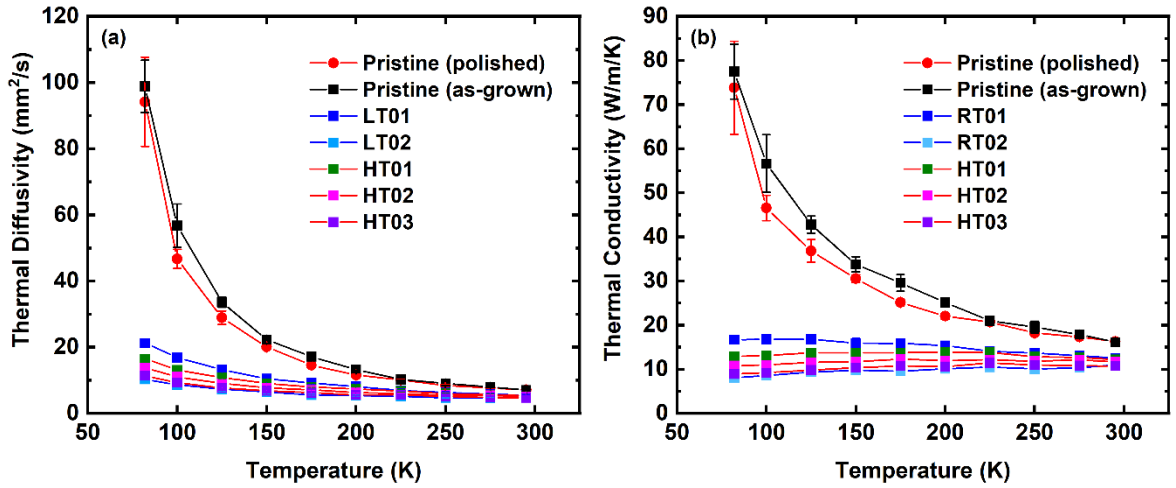

Fig. 5. (a) Thermal diffusivity and (b) thermal conductivity as a function of temperature measured on pristine and irradiated ThO_2 using SDTR [67].

Figs. 6(a) and (b) illustrate the reduction in thermal conductivity with applied dose at 82 K and at 300 K, respectively. A drastic reduction of ~89% is seen in the thermal conductivity at 82 K from the pristine sample to sample RT02 (0.01 dpa at room temperature). The reduction in the thermal conductivity at room temperature between the two samples is ~32%. Our measurements also show a monotonic decrease in the thermal conductivity from the pristine sample to samples RT01 and RT02. This trend shows that our measurements capture the degradation of thermal conductivity at the early stages of damage accumulation at low dose levels. The microstructure of the ThO_2 samples irradiated at room temperature is expected to be dominated by point defects that act as strong scatterers of phonons. It is expected that point defects are primarily responsible for the large reduction in thermal conductivity in samples RT01 and RT02. Although samples RT02 and HT01 were irradiated to the same dose level (albeit at different irradiation temperatures), the thermal conductivity of HT01 is ~60% higher than that of RT02 at 82 K, and ~11% higher at 300 K. A higher thermal conductivity of samples irradiated at elevated temperature when compared to the corresponding thermal conductivity of samples irradiated to the same dose at room temperature was reported previously for higher-dose irradiated ThO_2 crystals [5] and was attributed to the combined effect of point defect recombination and clustering into extended defects such as dislocation loops due to the higher mobility of point defects at elevated temperature. The thermal conductivity of the samples irradiated

at 600°C also exhibits a reduction with dose. However, the slope of this dose-dependent reduction is not as steep as that seen in the room temperature-irradiated samples. Our TEM observations indicate the presence of dislocation loops in the microstructure of the 600°C irradiated samples consistent with the expected clustering. These defect clusters are expected to scatter phonons to a lesser extent than atomic-scale point defects.

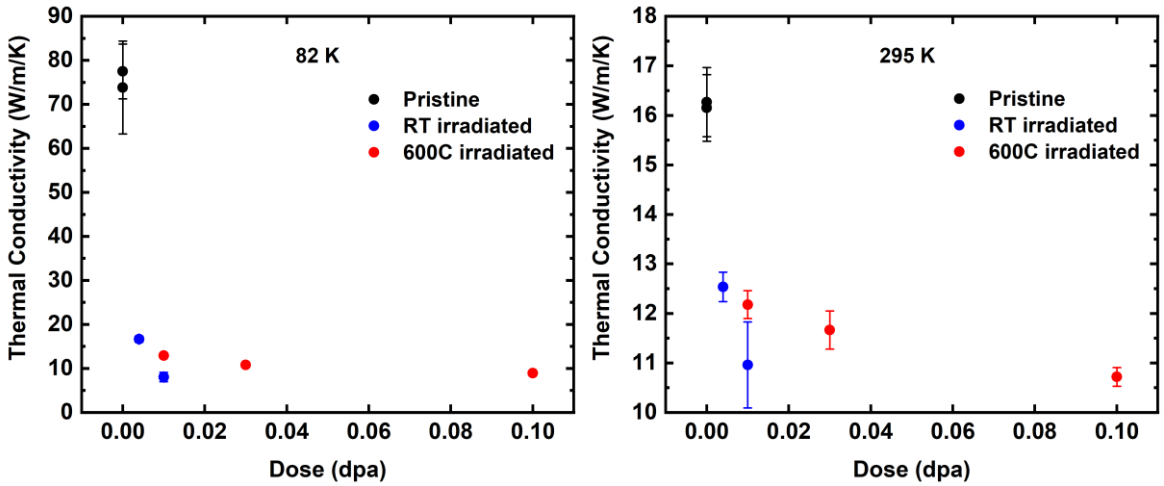

Fig. 6. Thermal conductivity as function of plateau region radiation dose in dpa in single crystal ThO_2 at 82 K (left) and at 295 K (right).

3.2 Defect cluster evolution

The cluster dynamics model described in Section 2.2 with its optimized set of parameters has been used to predict the density of monomers and SIA loops, particularly small loops with radii less than 1 nm, in ThO_2 irradiated at 600°C up to a dose of 0.1 dpa. Fig. 7(a) gives the evolution of loop size distribution with dose. We see a typical size distribution function (SDF) with a high density of Th_i and O_i monomers, Th_i-O_i dimers and very small loops followed by the density distribution of small and large loops. The distribution peaks at an intermediate size which shifts to larger sizes with the progress of irradiation, indicating loop growth. The high density of monomers and very small loops drive the kinetics of loop growth. As shown in Fig. 7(b), the predicted loop density distribution compares closely with the TEM observations. The total loop density predicted by CD increases steeply at low doses and saturates very quickly [Fig. 7(c)]. This is characteristic of loop growth as we expect large loops to grow at the expense of small ones. The observed density in TEM also follows a similar trend. However, the measured total densities at different doses are

about three times less than the CD predictions even when they are of the same order of magnitude. This discrepancy is primarily attributed to the limited resolution of TEM that makes it difficult to visualize and hence accurately estimate the density of small loops, i.e. loops having radius smaller than 1 nm. The plots in Figs. 7(c-d) also include data for large dose samples previously reported in [31]. The error associated with the CD parameters may also be a reason for overpredicting the total loop density. The evolution of average loop radius with dose, shown in Fig. 7(d), is accurately predicted by CD as it is within the TEM error limits.

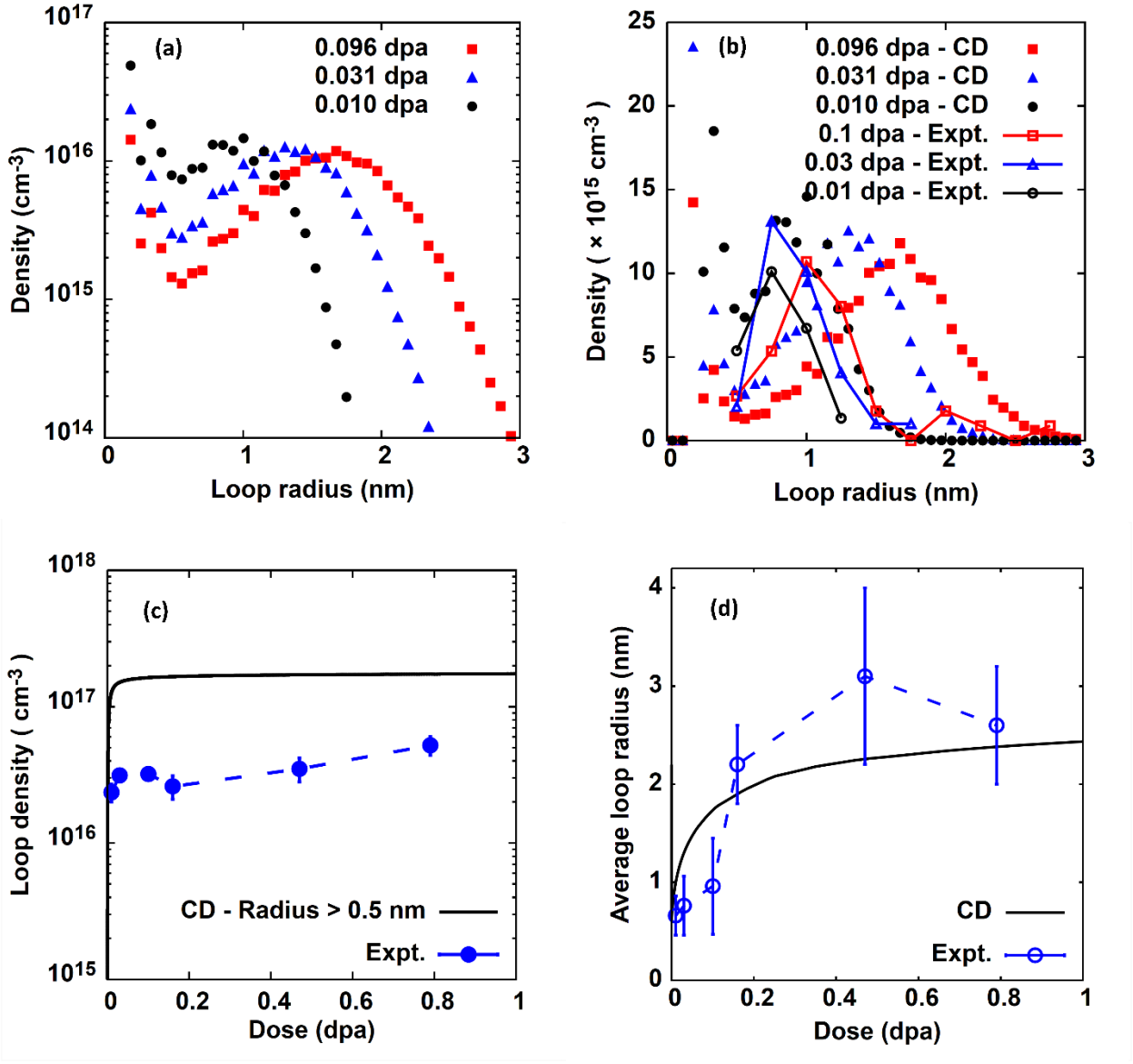

Fig. 7(a) Evolution of the size distribution function (SDF) of SIA loops on irradiation at 600ºC, predicted by CD. (b) SDF of SIA loops predicted by CD in comparison with TEM observations. (c) Comparision of the CD predicted total density of loops having radius > 0.5 nm with the total loop density measured from TEM. (d) Variation of the average loop radius with dose predicted by CD in comparison with TEM observations. The TEM observed loop densities and average radii at high irradiation doses shown in (c) and (d) are taken from [31].

Fig. 8(a) and (c) shows the variation of individual monomer and dimer densities predicted by CD at irradiation temperatures of 30ºC and 600ºC respectively. At 30ºC which is close to the room temperature, there is a significant accumulation of monomers in the matrix. This is a consequence of low point defect diffusivities that impede the migration of monomers and their interaction with defect sinks and other clusters. Also, CD predicts the nucleation and accumulation of SIA dimers and small loops, whereas the growth of large loops is restricted due to limited defect mobilities. On further irradiation, O_i being the most mobile defect species in the ThO_2 matrix, starts depleting in density as seen in Fig. 8(a) due to two separate interactions, i.e., migration of O_i to V_O resulting in recombination and the generation of small loops with Th_i and Th_i-O_i dimers. Recombination results in a slight depletion of V_O whereas nucleation of small loops reduce the Th_i and dimer densities by small amount. This is evident from the kinks in the plot of V_O and Th_i densities and the change in slope of the dimer density plot respectively in Fig. 8(a). As discussed in the Section 3.1, The PL peaks and optical absorption bands at 1.67 eV and 1.95 eV are consistent with previous observations in ThO_2 single crystals irradiated with energetic protons to higher plateau damage dose levels of up to 0.79 dpa [37]. Using DFT calculations, the PL peak at 1.67 eV was attributed to new electronic transitions created by electrons trapped at neutral oxygen vacancies, while that at 1.95 eV was attributed to electronic transitions from positively-charged oxygen vacancies [37]. CD predicts an accumulation of V_O with irradiation dose at 30ºC as shown in Fig. 8(b) which is consistent with the trend in measured intensity of PL peaks at 1.67 and 1.95 eV.

At high irradiation temperature of 600ºC, there is an accumulation of monomers at very small doses followed by depletion of O_i in the matrix owing to its migration, recombination with V_O, and clustering with Th_i to form dimers and very small loops as shown in Fig. 8(c). Th_i being comparatively less mobile than O_i keeps accumulating further. Recombination with O_i slightly depletes the density of V_O, indicated

by a kink in the plot of V_O density. However, it keeps increasing steadily with dose until it begins clustering with V_{Th} to form vacancy dimers and small voids. Finally, as irradiation proceeds, Th_i becomes mobile and starts recombining with V_{Th}. This depletes the density of V_{Th} in the matrix slightly while steadily accumulating with dose. The sluggish kinetics of V_{Th} migration also restricts the growth of large voids which is consistent with the TEM observations by Dennett et al. [31]. Also, enhanced Th_i migration results in SIA loop growth in the irradiated matrix. Our CD results indicate that the density of oxygen vacancies decreases with irradiation dose, shown in Fig. 8(d), owing to vacancies clustering into V_{Th}-V_O dimers and small voids. The trend in measured intensity of the PL peak at 1.95 eV with dose qualitatively follows the CD model predictions. This trend is also seen in the amplitude of the optical absorption oscillator at 1.95 eV, albeit with a larger scatter. Thus, results from our CD model seems to correspond well with experimental observations and consequently can be used to predict the density of point defects and small clusters unresolved in TEM with high fidelity. Further development of CD models that consider electron trapping and discriminating between charged and neutral vacancies, when coupled with the optical spectroscopy techniques used here, may provide further insight into the evolution of point defects at the early stages of damage accumulation.

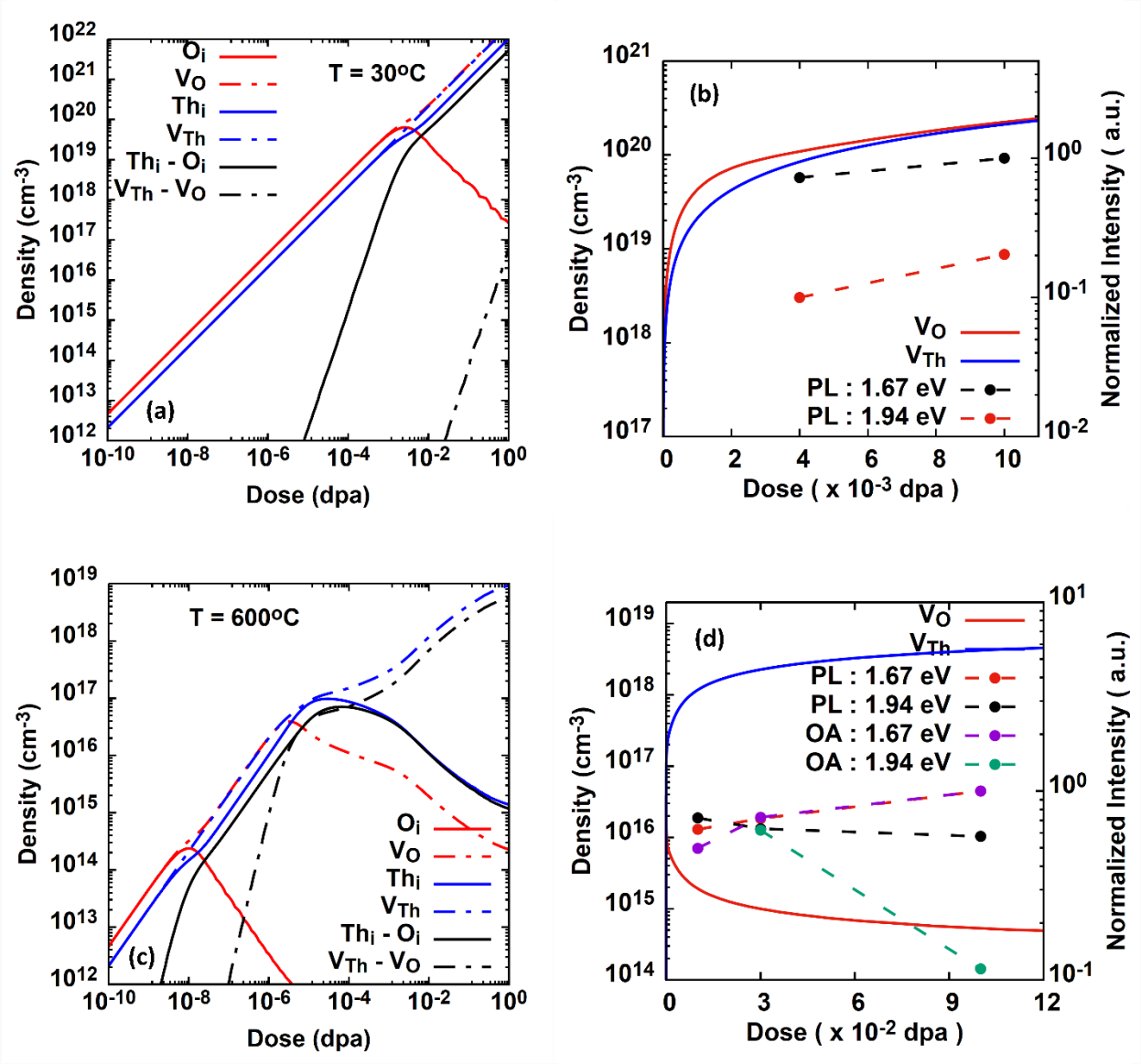

Fig. 8. Evolution of the monomer density and the density of SIA and vacancy dimers, predicted by CD at (a) 30°C and (c) 600°C. Density of vacancy monomers and dimers plotted with irradiation dose at (b) 30°C ~ room temperature and (d) 600°C. Amplitude of the peaks obtained from PL and optical absorption spectroscopy of irradiated ThO_2, plotted with irradiation dose.

3.3 Thermal conductivity predictions

Fig. 9 shows BTE modeling results for temperature-dependent thermal conductivity of ThO_2 compared with experimentally measured values for both the pristine sample and LT-series samples, irradiated at room temperature to 0.004 dpa (a) and 0.01 dpa (b). CD results do not predict evolution of point defects into

sufficient concentrations of larger vacancy and interstitial clusters to effect thermal conductivity and so their effect on thermal conductivity is not plotted here. The black and red curves show our model results for pristine and irradiated ThO_2, respectively. All other curves show the resultant thermal conductivity reduction when only one defect type has been introduced to the model. For both 0.004 and 0.01 dpa, V_{Th} and Th_I are the most significant contributors to the reduction in conductivity of the irradiated fuel due to their higher concentrations [Fig. 9(a)] and their much higher mass when compared to O defects. Furthermore, because of their higher concentrations, V_{Th} result in the largest reduction of conductivity of all defects. Dimer interstitial defects also cause significant reduction in conductivity due to their appreciable concentrations as O defects easily migrate to nearby Th defects. This can also be seen when comparing O defect conductivity reductions as both V_O and O_I contribute less percentage of conductivity reduction at higher dpa. Predicted conductivities for the LT-series samples at each dpa are quite good at temperatures above 150K, especially considering the simplicity of the phonon scattering models implemented. One question that the LT01 [Fig. 9(a)] result raises, however, is the deviation from the temperature trend below 150K. There seems to be important physics not captured at low temperatures by the currently implemented Rayleigh scattering from point defects [57], since the conductivity reduction of our LT-series model depends solely on point defect scattering. The effect is made more noticeable in the LT02 [Fig. 9(a)] result in which point defect concentrations have increased, and the trend is made more apparent. This result highlights the need for better understanding of phonon scattering mechanisms in irradiated oxides at low temperatures.

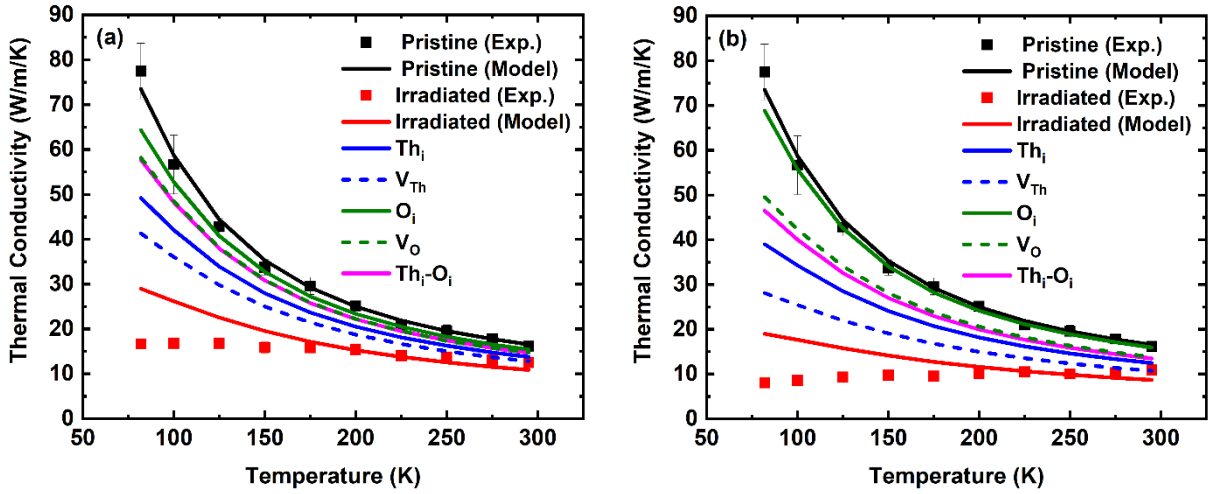

Fig. 9. Modeled temperature dependent thermal conductivity of ThO_2 samples irradiated at room temperature and compared to experimentally measured values for LT01 – 0.004 dpa (a) and LT02 – 0.01 dpa (b).

Fig. 10 presents BTE modeling results for temperature dependent thermal conductivity of ThO_2 compared with experimentally measured values for the pristine sample and samples HT01, HT02, and HT03 irradiated at 600 ℃ to 0.01, 0.03, and 0.1 dpa, respectively. At the elevated irradiation temperature, the generated point defects now have increased mobility and nucleate to grow voids and dislocation loops in substantial concentrations and size. In all three figures, the "Point Defects" line represents the contribution from all monomers and dimers. As predicted by our CD results, we see for the HT-series samples that point defects have a near-negligible effect on conductivity reduction, since most have contributed in the growth of voids and loops. Although the voids ("Vacancy Clusters" curves) cause an appreciable reduction in conductivity, in all HT-series samples we see the total conductivity reduction governed almost solely by the concentration of dislocation loops ("Interstitial Clusters" curves). Comparing results of the high and low temperature irradiated samples at the same dose rate (LT02 and HT01 - 0.01 dpa), we see a recovery of the high temperature sample. This recovery is characterized by the migration of point defects to loops and voids, and thus, reducing the overall scattering cross-section. Similar to the LT-series model results, the HT01 model for thermal conductivity agrees extremely well with measured values at temperatures above roughly 175 K but deviates significantly at lower temperatures. Again, this motivates future work to investigate other possible scattering mechanisms in irradiated fuels at low temperatures. Considering the HT02 model

results, we see that this substantial deviation in predicted conductivity at low temperature is gone, and the model results seem to have be nearing a saturation in conductivity, as are the experimentally-measured results. However, like the LT-series samples, the measured results for HT-series samples seem to exhibit a recovery in conductivity at higher temperatures that our model cannot predict. For the HT03 sample, we now see that the model results are significantly lower than measured values of thermal conductivity. This exhibits our CD model predictions [Fig. 7(a)] which demonstrate an increasing concentration of larger dislocation loops at higher dose since the scattering rate for the loops [Eq. (8)] are inversely to both loop radius squared and the concentration. This discrepancy could likely be due to limitations in the relaxation time model [63] used for the loops, where it is assumed that all loops are oriented normal to the temperature gradient and could be too restrictive of an assumption.

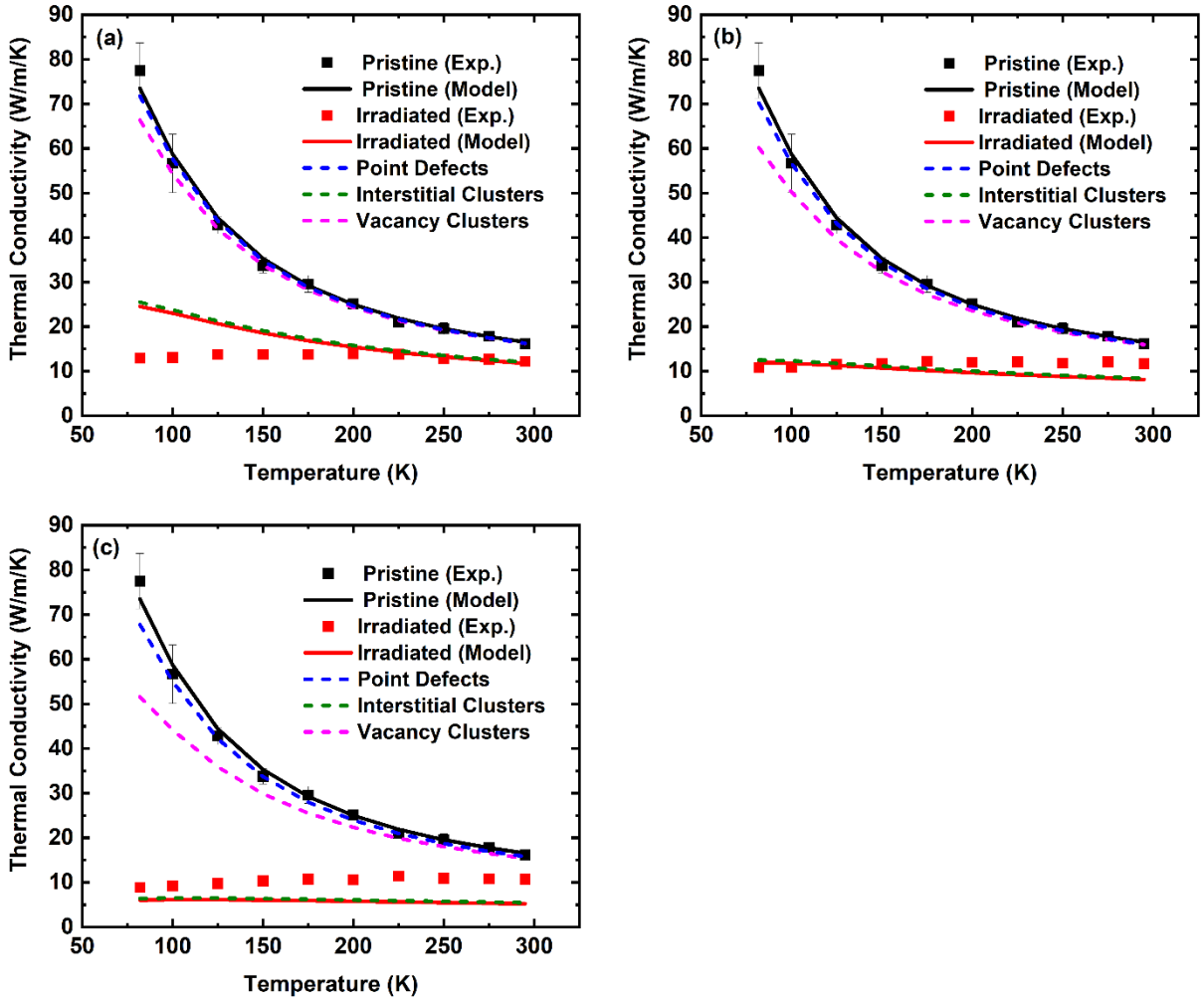

Fig. 10. Modeled temperature dependent thermal conductivity of ThO_2 samples irradiated at 600 ℃ and compared to experimentally measured values for HT01 – 0.01 dpa (a), HT02 – 0.03 dpa (b), and HT03 – 0.1 dpa (c).

In Fig. 11, BTE modeling results at constant temperatures of 82 and 295 K are compared to experimentally-measured thermal conductivity as a function of proton radiation dose. In reference to the room temperature (RT) irradiated samples, where the phonon scattering is determined predominately by point defects, we see overprediction and slight underprediction in thermal conductivity at 82 K and 295 K, respectively, with the largest discrepancy being at 82 K. This again emphasizes conclusions drawn from Fig. 9, that modeling thermal conductivity of irradiated fuels can be done reasonably well at higher temperatures, but further physics insight is needed to understand the influence of point defects on thermal conductivity at lower temperatures. The results are a bit less desirable for the HT-series samples at 295 K and irradiated at 600 ℃, where we see substantial underprediction of thermal conductivity by our model compared to experiment. As previously mentioned, this substantial underprediction could be result of the thermal conductivity being predominately controlled by dislocation loops and too restrictive of assumptions made in the phonon-loop relaxation time model [Eq. (8)]. The continued decrease of conductivity with increasing radiation dose is expected as the increase in monomer defects drive loop growth, and the phonon-loop relaxation time model predicts increased phonon scattering rates proportional to the loop concentration and the loop radius squared. However, as evident again in Fig. 11, at 295 K the HT-series samples seem to have reached near-saturation levels, while model predictions are still evolving. As mentioned previously, this highlights the need for further work on the mechanisms affecting thermal transport in irradiated fuels.

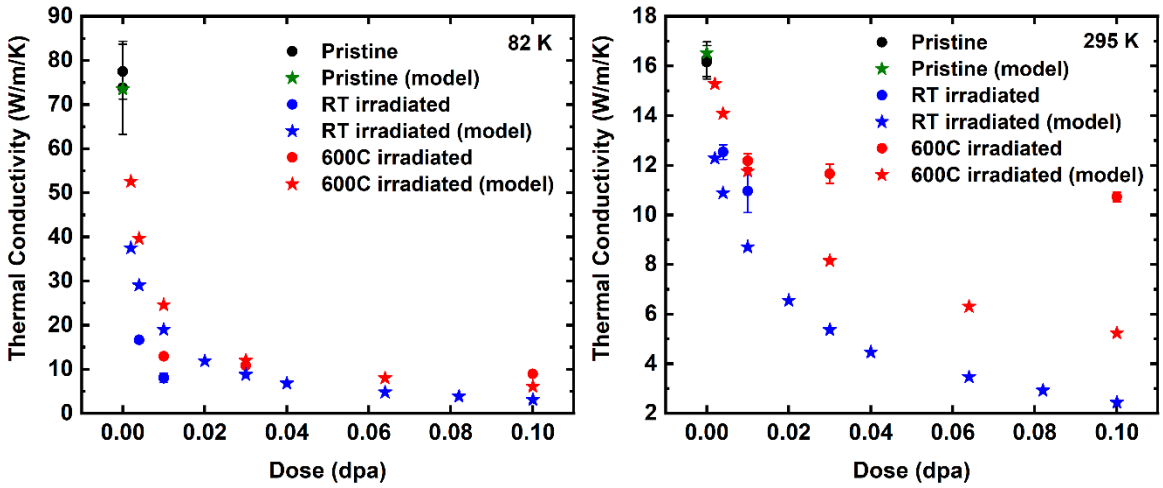

Fig. 11. Predicted (star symbols) and measured (circle symbols) thermal conductivity at 82 K (left) and 295 K (right) versus dose rate of ThO_2 irradiated at room temperature (RT) and 600 ℃.

4. Discussion

With thermal conductivity being one of the most important performance metrics of nuclear fuels, the present communication aims to further the understanding of thermal conductivity reduction of fuels upon irradiation by using thorium dioxide as a model system. The previous work by Dennett et al. [31] was a first step in characterizing this reduction in conductivity by integrating experimental measurements and theoretical predictions into a comprehensive framework for investigating thermal conductivity in a defect-bearing actinide oxide like thorium dioxide. As previously mentioned, the present communication is aimed to be an extension of the work by Dennett and coworkers. This was achieved by expanding the range of irradiation conditions of the ThO_2 samples, using lower dose irradiation conditions such that the dependence of conductivity reduction on applied dose is further illuminated, and implementing a cluster dynamics model allowing the prediction of lattice defects ranging in size from point defects to extended defects such as voids and dislocation loops. Like the previous study, the temperature dependence of thermal conductivity was investigated below room temperature as to discriminate between phonon scatterings by lattice defects and those by 3-phonon processes which dominate at higher temperatures.

For ThO_2 specimens irradiated at room temperature (LT-series), we find the lattice defect population to be composed primarily of point defects. At this lower irradiation temperature, the generated point defects do not have sufficient mobility to migrate into larger defects like voids and loops of significant concentrations. Our modeling results for these LT-series samples [Fig. (9)] show the largest contributors to thermal conductivity reduction being attributed to thorium vacancies and interstitials, in that order. This is due in part by i) lower mobility and recombination rates of thorium defects which promotes larger concentrations and ii) larger mass of thorium defects compared to those for oxygen resulting in larger phonon scattering cross-section. Our predicted temperature-dependent thermal conductivity for the LT-series samples agree well with experimentally measured values for temperatures above 150 K. However, at lower temperatures we see an increasing deviation from measured values. This seems to be a scattering mechanism from point defects at lower temperature that is not captured by the current BTE modeling. A possibility here is a resonant-type scattering mechanism which scatters phonons of frequencies near the defect's resonant frequency more strongly. Depending on the resonant frequency, this could lead to the observed decrease in thermal conductivity at low temperatures. Another consideration is how well the strong assumptions made in the Klemens point defect model can approximate phonon scattering which includes dispersion and optical modes. Both of these possible reason for discrepancies between the modeled and measured thermal conductivities at lower temperatures warrant future investigation.

Comparing the measured thermal conductivities of the LT-series sample and the HT-series sample subjected to the same radiation dose of 0.01 dpa [Fig. 9(b) and Fig. 10(a) respectively], we observe recovery in conductivity in the HT sample. The is evident of a reduction in phonon scattering sites as the point defects have migrated and clustered into voids and loops. This same effect is also captured by our model results for the HT-series samples found in Fig. 10 where the predicted reduction in conductivity is nearly completely determined by the clustering of interstitial defects to form dislocation loops. However, the measured conductivities for the HT-series samples seem to have reach a saturation level where any further microstructural change has minimal effect of the on the conductivity. Furthermore, the temperature

dependence in the conductivity for these samples peaks above 150 K, a trend not possible with the current scattering model. The reason for these two discrepancies could be a future work.

5. Concluding Remarks

A comprehensive experimental and theoretical approach has been used to better understand phonon-mediated thermal transport in low-dose irradiated thorium dioxide. Temperature-dependent thermal conductivity of proton irradiated ThO_2 is predicted using a Boltzmann transport equation framework for phonons in the single-mode relaxation time approximation. Contributions to the total phonon relaxation time include intrinsic 3-phonon and native impurity scattering, as well as proton irradiation induced defects including point defects, voids, and dislocation loops. Concentrations and sizes of extrinsic defects are calculated as a function of irradiation temperature and dose using an atomistically-informed cluster dynamics model which captures the nucleation and growth of defect clusters in the irradiated matrix. The results of the CD model are compared to direct TEM measurements of proton irradiated samples then feed to the BTE algorithm for calculation of frequency dependent phonon relaxation times within a 3D treatment of the FCC Brillouin zone. In general, agreement between the model and experimental measurements of thermal conductivity are quite good, despite the model's use of only a single-fitting parameter to capture conductivity reduction due to intrinsic impurities of the ThO_2 samples. However, conductivity saturation is observed in the experimental measurements while the models defect population shows continued evolution. Furthermore, a reduction of conductivity observed at low temperatures was not adequately captured by the model, despite very good agreement at high temperatures. This seems evident of point defect complexities which are not accounted for in the current phonon scattering algorithm and signify physics which are not captured by the current phonon scattering model. An improvement of the scattering model for point defects could be inclusion of resonance scattering by charged F-center defects as opposed to the uncharged oxygen vacancy model implemented currently. Furthermore, experimental characterization of other small-scale defects through Raman spectroscopy for comparison with the current CD model could shed light on inadequacies of the current modeling algorithm.

Acknowledgments

This work was supported by the Center for Thermal Energy Transport under Irradiation (TETI), an Energy Frontier Research Center funded by the US Department of Energy, Office of Science, Office of Basic Energy Sciences.

References

[1] P.E. MacDonald, C.B. Lee, Use of thoria-urania fuels in PWRs: A general review of a NERI project to assess feasible core designs, economics, fabrication methods, in-pile thermal/mechanical behavior, and waste form characteristics, Nuclear Technology. 147 (2004) 1–7. https://doi.org/10.13182/NT04-A3510.

[2] D. Das, S.R. Bharadwaj Editors, Green Energy and Technology Thoria-based Nuclear Fuels Thermophysical and Thermodynamic Properties, Fabrication, Reprocessing, and Waste Management, n.d. http://www.springer.com/series/8059.

[3] M. Mann, D. Thompson, K. Serivalsatit, T.M. Tritt, J. Ballato, J. Kolis, Hydrothermal growth and thermal property characterization of ThO 2 single crystals, Crystal Growth and Design. 10 (2010) 2146–2151. https://doi.org/10.1021/cg901308f.

[4] C. Ronchi, M. Sheindlin, D. Staicu, M. Kinoshita, Effect of burn-up on the thermal conductivity of uranium dioxide up to 100.000 MWdt-1, Journal of Nuclear Materials. 327 (2004) 58–76. https://doi.org/10.1016/j.jnucmat.2004.01.018.

[5] C.A. Dennett, Z. Hua, A. Khanolkar, T. Yao, P.K. Morgan, T.A. Prusnick, N. Poudel, A. French, K. Gofryk, L. He, L. Shao, M. Khafizov, D.B. Turner, J.M. Mann, D.H. Hurley, The influence of lattice defects, recombination, and clustering on thermal transport in single crystal thorium dioxide, APL Materials. 8 (2020). https://doi.org/10.1063/5.0025384.

[6] X.Y. Liu, M.W.D. Cooper, K.J. McClellan, J.C. Lashley, D.D. Byler, B.D.C. Bell, R.W. Grimes, C.R. Stanek, D.A. Andersson, Molecular Dynamics Simulation of Thermal Transport in UO2 Containing Uranium, Oxygen, and Fission-product Defects, Physical Review Applied. 6 (2016). https://doi.org/10.1103/PhysRevApplied.6.044015.

[7] D.H. Hurley, A. El-Azab, M.S. Bryan, M.W.D. Cooper, C.A. Dennett, K. Gofryk, L. He, M. Khafizov, G.H. Lander, M.E. Manley, J.M. Mann, C.A. Marianetti, K. Rickert, F.A. Selim, M.R. Tonks, J.P. Wharry, Thermal Energy Transport in Oxide Nuclear Fuel, Chemical Reviews. 122 (2022). https://doi.org/10.1021/acs.chemrev.1c00262.

[8] L.K. Mansur, Theory and experimental background on dimensional changes in irradiated alloys, Journal of Nuclear Materials. 216 (1994) 97–123. https://doi.org/10.1016/0022-3115(94)90009-4.

[9] A. Hardouin Duparc, C. Moingeon, N. Smetniansky-de-Grande, A. Barbu, Microstructure modelling of ferritic alloys under high flux 1 MeV electron irradiations, Journal of Nuclear Materials. 302 (2002) 143–155. https://doi.org/10.1016/S0022-3115(02)00776-6.

[10] A. Gokhman, F. Bergner, Cluster dynamics simulation of point defect clusters in neutron irradiated pure iron, Radiation Effects and Defects in Solids. 165 (2010) 216–226. https://doi.org/10.1080/10420151003631928.

[11] F. Christien, A. Barbu, Effect of self-interstitial diffusion anisotropy in electron-irradiated zirconium: A cluster dynamics modeling, Journal of Nuclear Materials. 346 (2005) 272–281. https://doi.org/10.1016/j.jnucmat.2005.06.024.

[12] C. Pokor, Y. Brechet, P. Dubuisson, J.-P. Massoud, A. Barbu, Irradiation damage in 304 and 316 stainless steels: experimental investigation and modeling. Part I: Evolution of the microstructure, Journal of Nuclear Materials. 326 (2004) 19–29. https://doi.org/10.1016/j.jnucmat.2003.11.007.

[13] D. Brimbal, L. Fournier, A. Barbu, Cluster dynamics modeling of the effect of high dose irradiation and helium on the microstructure of austenitic stainless steels, Journal of Nuclear Materials. 468 (2016) 124–139. https://doi.org/10.1016/j.jnucmat.2015.11.007.

[14] T. Faney, B.D. Wirth, Spatially dependent cluster dynamics modeling of microstructure evolution in low energy helium irradiated tungsten, Model Simul Mat Sci Eng. 22 (2014) 65010–17. https://doi.org/10.1088/0965-0393/22/6/065010.

[15] R. Skorek, G. Carlot, S. Maillard, A. Michel, T. Jourdan, E. Gilabert, Modelling Fission Gas Bubble Distribution in UO2, Diffusion and Defect Data. Solid State Data. Pt. A, Defect and Diffusion Forum. 323–325 (2012) 209–214. https://doi.org/10.4028/www.scientific.net/DDF.323-325.209.

[16] C. Matthews, R. Perriot, M.W.D. Cooper, C.R. Stanek, D.A. Andersson, Cluster dynamics simulation of uranium self-diffusion during irradiation in UO2, Journal of Nuclear Materials. 527 (2019) 151787. https://doi.org/10.1016/j.jnucmat.2019.151787.

[17] C. Matthews, R. Perriot, M.W.D. Cooper, C.R. Stanek, D.A. Andersson, Cluster dynamics simulation of xenon diffusion during irradiation in UO2, Journal of Nuclear Materials. 540 (2020) 152326. https://doi.org/10.1016/j.jnucmat.2020.152326.

[18] S. Khalil, T. Allen, A. EL-Azab, Off-stoichiometric defect clustering in irradiated oxides, Chem Phys. 487 (2017) 1–10. https://doi.org/10.1016/j.chemphys.2017.01.014.

[19] S. Mazumder, M. Singh, T. Kumagai, A. El-Azab, Atomistically-informed modeling of point defect clustering and evolution in irradiated ThO2, arXiv:2206.06500, June 2022.

[20] K. Bawane, X. Liu, T. Yao, M. Khafizov, A. French, J.M. Mann, L. Shao, J. Gan, D.H. Hurley, L. He, TEM characterization of dislocation loops in proton irradiated single crystal ThO2, Journal of Nuclear Materials. 552 (2021). https://doi.org/10.1016/j.jnucmat.2021.152998.

[21] L. He, T. Yao, K. Bawane, M. Jin, C. Jiang, X. Liu, W. Chen, J.M. Mann, D.H. Hurley, J. Gan, M. Khafizov, Dislocation loop evolution in Kr-irradiated ThO_2, Journal of the American Ceramic Society. (2022). https://doi.org/10.1111/jace.18478.

[22] Y. Miao, D. Aidhy, W.Y. Chen, K. Mo, A. Oaks, D. Wolf, J.F. Stubbins, The evolution mechanism of the dislocation loops in irradiated lanthanum doped cerium oxide, Journal of Nuclear Materials. 445 (2014). https://doi.org/10.1016/j.jnucmat.2013.11.015.

[23] D.A. Broido, M. Malorny, G. Birner, N. Mingo, D.A. Stewart, Intrinsic lattice thermal conductivity of semiconductors from first principles, Applied Physics Letters. 91 (2007). https://doi.org/10.1063/1.2822891.

[24] L. Lindsay, D.A. Broido, T.L. Reinecke, Ab initio thermal transport in compound semiconductors, Physical Review B - Condensed Matter and Materials Physics. 87 (2013). https://doi.org/10.1103/PhysRevB.87.165201.

[25] B. Szpunar, J.A. Szpunar, K.S. Sim, Theoretical investigation of structural and thermo-mechanical properties of thoria, Journal of Physics and Chemistry of Solids. 90 (2016) 114–120. https://doi.org/10.1016/j.jpcs.2015.10.011.

[26] H. Nakamura, M. Machida, First-principles calculation study on phonon thermal conductivity of thorium and plutonium dioxides: Intrinsic anharmonic phonon-phonon and extrinsic grain-boundary–phonon scattering effects, Journal of Nuclear Materials. 519 (2019) 45–51. https://doi.org/10.1016/j.jnucmat.2019.03.033.

[27] M.W.D. Cooper, S.C. Middleburgh, R.W. Grimes, Modelling the thermal conductivity of (UxTh1-x)O2 and (UxPu1-x)O2, Journal of Nuclear Materials. 466 (2015) 29–35. https://doi.org/10.1016/j.jnucmat.2015.07.022.

[28] J. Park, E.B. Farfán, K. Mitchell, A. Resnick, C. Enriquez, T. Yee, Sensitivity of thermal transport in thorium dioxide to defects, Journal of Nuclear Materials. 504 (2018) 198–205. https://doi.org/10.1016/j.jnucmat.2018.03.043.

[29] M.J. Rahman, B. Szpunar, J.A. Szpunar, Dependence of thermal conductivity on fission-product defects and vacancy concentration in thorium dioxide, Journal of Nuclear Materials. 532 (2020). https://doi.org/10.1016/j.jnucmat.2020.152050.

[30] M. Khafizov, V. Chauhan, Y. Wang, F. Riyad, N. Hang, D.H. Hurley, Investigation of thermal transport in composites and ion beam irradiated materials for nuclear energy applications, Journal of Materials Research. 32 (2017) 204–216. https://doi.org/10.1557/jmr.2016.421.

[31] C.A. Dennett, W.R. Deskins, M. Khafizov, Z. Hua, A. Khanolkar, K. Bawane, L. Fu, J.M. Mann, C.A. Marianetti, L. He, D.H. Hurley, A. El-Azab, An integrated experimental and computational investigation of defect and microstructural effects on thermal transport in thorium dioxide, Acta Materialia. 213 (2021). https://doi.org/10.1016/j.actamat.2021.116934.

[32] L. He, M. Khafizov, C. Jiang, B. Tyburska-Püschel, B.J. Jaques, P. Xiu, P. Xu, M.K. Meyer, K. Sridharan, D.P. Butt, J. Gan, Phase and defect evolution in uranium-nitrogen-oxygen system under irradiation, Acta Materialia. 208 (2021). https://doi.org/10.1016/j.actamat.2021.116778.

[33] W.R. Deskins, A. Hamed, T. Kumagai, C.A. Dennett, J. Peng, M. Khafizov, D. Hurley, A. El-Azab, Thermal conductivity of ThO2: Effect of point defect disorder, Journal of Applied Physics. 129 (2021). https://doi.org/10.1063/5.0038117.

[34] J.F. Ziegler, M.D. Ziegler, J.P. Biersack, SRIM - The stopping and range of ions in matter (2010), Nuclear Instruments and Methods in Physics Research, Section B: Beam Interactions with Materials and Atoms. 268 (2010) 1818–1823. https://doi.org/10.1016/j.nimb.2010.02.091.

[35] W.J. Weber, Y. Zhang, Predicting damage production in monoatomic and multi-elemental targets using stopping and range of ions in matter code: Challenges and recommendations, Current Opinion in Solid State and Materials Science. 23 (2019). https://doi.org/10.1016/j.cossms.2019.06.001.

[36] H.Y. Xiao, Y. Zhang, W.J. Weber, Ab initio molecular dynamics simulations of low-energy recoil events in ThO 2, CeO 2, and ZrO 2, Physical Review B - Condensed Matter and Materials Physics. 86 (2012). https://doi.org/10.1103/PhysRevB.86.054109.

[37] A. Khanolkar, C.A. Dennett, Z. Hua, J.M. Mann, D.H. Hurley, M. Khafizov, Inferring relative dose-dependent color center populations in proton irradiated thoria single crystals using optical spectroscopy, Phys Chem Chem Phys. 24 (2022) 6133–6145. https://doi.org/10.1039/d1cp05191a.

[38] D.H. Hurley, R.S. Schley, M. Khafizov, B.L. Wendt, Local measurement of thermal conductivity and diffusivity, Review of Scientific Instruments. 86 (2015). https://doi.org/10.1063/1.4936213.

[39] Z. Hua, H. Ban, M. Khafizov, R. Schley, R. Kennedy, D.H. Hurley, Spatially localized measurement of thermal conductivity using a hybrid photothermal technique, in: Journal of Applied Physics, 2012. https://doi.org/10.1063/1.4716474.

[40] M. Reichling, H. Grönbeck, Harmonic heat flow in isotropic layered systems and its use for thin film thermal conductivity measurements, Journal of Applied Physics. 75 (1994) 1914–1922. https://doi.org/10.1063/1.356338.

[41] S.J. Mason, D.J. Wesenberg, A. Hojem, M. Manno, C. Leighton, B.L. Zink, Violation of the Wiedemann-Franz law through reduction of thermal conductivity in gold thin films, Physical Review Materials. 4 (2020). https://doi.org/10.1103/PhysRevMaterials.4.065003.

[42] B. Szpunar, J.A. Szpunar, K.S. Sim, Theoretical investigation of structural and thermo-mechanical properties of thoria, Journal of Physics and Chemistry of Solids. 90 (2016) 114–120. https://doi.org/10.1016/j.jpcs.2015.10.011.

[43] M. Khafizov, I.-W. Park, A. Chernatynskiy, L. He, J. Lin, J.J. Moore, D. Swank, T. Lillo, S.R. Phillpot, A. El-Azab, D.H. Hurley, Thermal Conductivity in Nanocrystalline Ceria Thin Films, Journal of the American Ceramic Society. 97 (2014) 562–569. https://doi.org/10.1111/jace.12673.

[44] K. Iakoubovskii, K. Mitsuishi, Y. Nakayama, K. Furuya, Thickness measurements with electron energy loss spectroscopy, Microscopy Research and Technique. 71 (2008) 626–631. https://doi.org/10.1002/jemt.20597.

[45] J. Gan, J.I. Cole, T.R. Allen, S. Shutthanandan, S. Thevuthasan, Irradiated microstructure of alloy 800H, Journal of Nuclear Materials. 351 (2006) 223–227. https://doi.org/10.1016/j.jnucmat.2006.02.009.

[46] S. Agarwal, T. Koyanagi, A. Bhattacharya, L. Wang, Y. Katoh, X. Hu, M. Pagan, S.J. Zinkle, Neutron irradiation-induced microstructure damage in ultra-high temperature ceramic TiC, Acta Materialia. 186 (2020) 1–10. https://doi.org/10.1016/j.actamat.2019.12.022.

[47] A. Etienne, M. Hernández-Mayoral, C. Genevois, B. Radiguet, P. Pareige, Dislocation loop evolution under ion irradiation in austenitic stainless steels, Journal of Nuclear Materials. 400 (2010) 56–63. https://doi.org/10.1016/j.jnucmat.2010.02.009.

[48] D. Chen, K. Murakami, K. Dohi, K. Nishida, Z. Li, N. Sekimura, The effects of loop size on the unfaulting of Frank loops in heavy ion irradiation, Journal of Nuclear Materials. 529 (2020) 151942. https://doi.org/10.1016/j.jnucmat.2019.151942.

[49] C.A. Schneider, W.S. Rasband, K.W. Eliceiri, NIH Image to ImageJ: 25 years of image analysis, Nat Methods. 9 (2012) 671–675. https://doi.org/10.1038/nmeth.2089.

[50] M. Jin, C. Jiang, J. Gan, D.H. Hurley, Systematic analysis on the primary radiation damage in Th 1 − x U x O 2 fluorite systems, Journal of Nuclear Materials. 536 (2020).

[51] K. Radhakrishnan, A.C. Hindmarsh, Description and Use of LSODE, the Livermore Solver for Ordinary Differential Equations, n.d.

[52] G.P. Srivastava, The physics of phonons, A. Hilger, Bristol ;, 1990.

[53] G.A. Slack, The Thermal Conductivity of Nonmetallic Crystals, in: Solid State Physics, Elsevier Science & Technology, 1979: pp. 1–71. https://doi.org/10.1016/S0081-1947(08)60359-8.

[54] A. Hamed, Computational modeling of thermal transport using spectral phonon Boltzmann transport equation, 2017.

[55] A. Hamed, A. El-Azab, Peak intrinsic thermal conductivity in non-metallic solids and new interpretation of experimental data for argon, Journal of Physics Communications. 2 (2018) 15022. https://doi.org/10.1088/2399-6528/aaa36f.

[56] K. Clausen, W. Hayes, J.E. Macdonald, R. Osborn, P.G. Schnabel, M.T. Hutchings, A. Magerl, Inelastic neutron scattering investigation of the lattice dynamics of ThO2 and CeO2, Journal of the Chemical Society, Faraday Transactions 2. 83 (1987) 1109. https://doi.org/10.1039/f29878301109.

[57] P.G. Klemens, The Scattering of Low-Frequency Lattice Waves by Static Imperfections, Proceedings of the Physical Society. Section A. 68 (1955) 1113–1128. https://doi.org/10.1088/0370-1298/68/12/303.

[58] Y. Lu, Y. Yang, P. Zhang, Thermodynamic properties and structural stability of thorium dioxide, Journal of Physics. Condensed Matter. 24 (2012) 225801–225801. https://doi.org/10.1088/0953-8984/24/22/225801.

[59] R. Gurunathan, R. Hanus, M. Dylla, A. Katre, G.J. Snyder, Analytical Models of Phonon–Point-Defect Scattering, Phys Rev Appl. 13 (2020). https://doi.org/10.1103/PhysRevApplied.13.034011.

[60] W. Kim, A. Majumdar, Phonon scattering cross section of polydispersed spherical nanoparticles, J Appl Phys. 99 (2006) 084306-084306–7. https://doi.org/10.1063/1.2188251.

[61] P.G. Klemens, Thermal Conductivity and Lattice Vibrational Modes, in: Solid State Physics, Elsevier Science & Technology, 1958: pp. 1–98. https://doi.org/10.1016/S0081-1947(08)60551-2.

[62] M. Khafizov, J. Pakarinen, L. He, D.H. Hurley, Impact of irradiation induced dislocation loops on thermal conductivity in ceramics, Journal of the American Ceramic Society. 102 (2019) 7533–7542. https://doi.org/10.1111/jace.16616.

[63] L.A. Turk, P.G. Klemens, Phonon scattering by impurity platelet precipitates in diamond, Physical Review. B, Solid State. 9 (1974) 4422–4428. https://doi.org/10.1103/PhysRevB.9.4422.

[64] A. Majumdar, Microscale Heat Conduction in Dielectric Thin Films, J Heat Transfer. 115 (1993) 7–16. https://doi.org/10.1115/1.2910673.

[65] A. Mock, C. Dugan, S. Knight, R. Korlacki, J.M. Mann, M.M. Kimani, J.C. Petrosky, P.A. Dowben, M. Schubert, Band-to-band transitions and critical points in the near-infrared to vacuum ultraviolet dielectric functions of single crystal urania and thoria, Appl Phys Lett. 114 (2019) 211901. https://doi.org/10.1063/1.5087059.

[66] T. Malis, S.C. Cheng, R.F. Egerton, EELS log-ratio technique for specimen-thickness measurement in the TEM, J Electron Microsc Tech. 8 (1988) 193–200. https://doi.org/10.1002/jemt.1060080206.

[67] E. Xiao, H. Ma, M.S. Bryan, L. Fu, J.M. Mann, B. Winn, D.L. Abernathy, R.P. Hermann, A.R. Khanolkar, C.A. Dennett, D.H. Hurley, M.E. Manley, C.A. Marianetti, Validating First-Principles Phonon Lifetimes via Inelastic Neutron Scattering, n.d.

Graphical Abstract

Impact of irradiation induced crystal defects on thermal transport in thorium dioxide

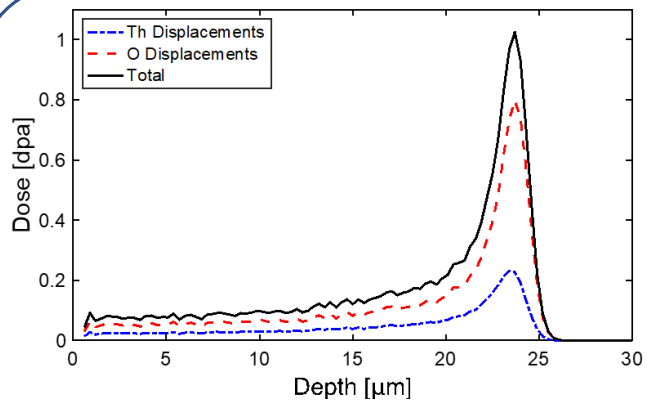

Generate defects in single crystal ThO_2 by irradiating samples with 2 MeV protons

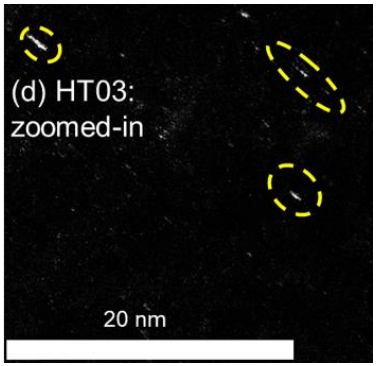

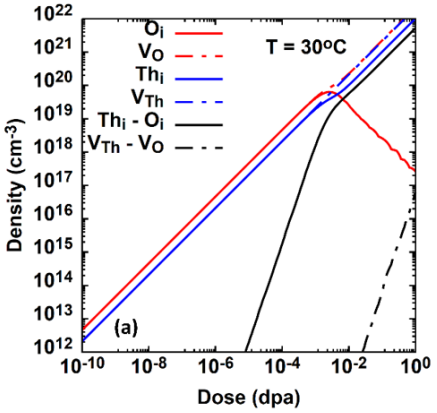

Measure defect densities via TEM measurements and cluster dynamics modeling

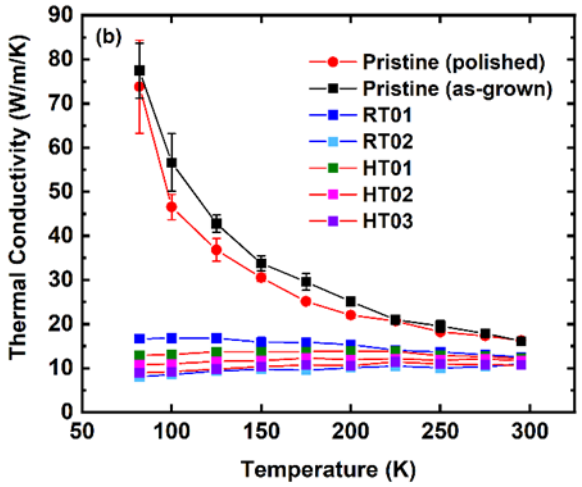

Measure temperature dependent thermal conductivity via thermoreflectance

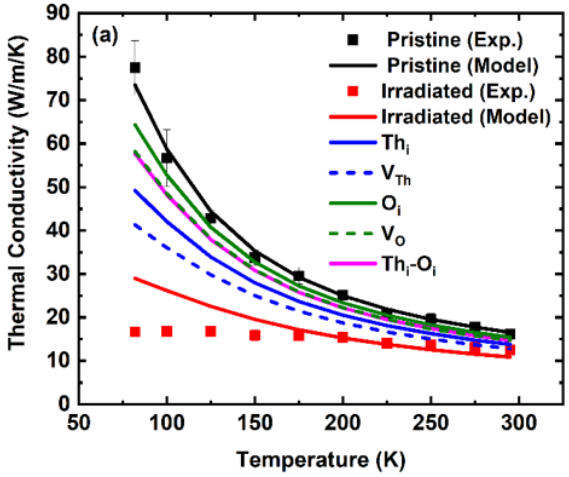

Use Boltzmann transport to model thermal conductivity reduction due to defects and compare with measurements

Declaration of interests

☒ The authors declare that they have no known competing financial interests or personal relationships that could have appeared to influence the work reported in this paper.

☐The authors declare the following financial interests/personal relationships which may be considered as potential competing interests: